INDEPENDENT COMPONENT ANALYSIS FOR GROUP COMPARISON OF FUNCTIONAL MRI IMAGES IN INDIVIDUALS WITH PARKINSON'S DISEASE

by

Kirsten Yaffe

A Thesis Submitted to the Faculty of the

DEPARTMENT OF EPIDEMIOLOGY AND BIOSTATISTICS

In Partial Fulfillment of the Requirements

For the Degree of

MASTER OF SCIENCE

WITH A MAJOR IN BIOSTATISTICS

In the Graduate College

THE UNIVERSITY OF ARIZONA

2020

THE UNIVERSITY OF ARIZONA
GRADUATE COLLEGE

As members of the Master's Committee, we certify that we have read the thesis prepared by: Kirsten Yaffe

titled: Independent Component Analysis For Group Comparison Of Functional MRI Images in Individuals with Parkinson's Disease

and recommend that it be accepted as fulfilling the thesis requirement for the Master's Degree.

Edward J Bedrick Date: 01/10/20

Ying-hui Chou Date: 01/10/2020

Chin-Hsien Hsu Date: 01/10/2020

Date: 1/10/2020

Final approval and acceptance of this thesis is contingent upon the candidate's submission of the final copies of the thesis to the Graduate College.

We hereby certify that we have read this thesis prepared under our direction and recommend that it be accepted as fulfilling the Master's requirement.

Edward J Bedrick Date: 01/10/20

Date: 1/10/20

Table of Figures

Abstract

Parkinson's Disease (PD) is an age-related disorder that affects cognitive and motor abilities and lowers quality of life. As there is currently no cure, it is an area of interest for many research efforts. Parkinson's disease has a substantial effect on structures in the basal ganglia, which may be used to indicate signs of Parkinson's disease progression.

Functional MRI (fMRI) is a means of measuring metabolic functioning in the brain. Brain imaging studies are not used to diagnose Parkinson's disease because it is unclear how it manifests in neuroimages. However, Parkinson's disease has a preclinical phase during which structures within the brain are affected, but external symptoms have not yet manifested. In this study, we sought to identify effects of Parkinson's disease that may be seen in functional imaging scans to allow earlier detection.

We used independent component analysis (ICA) to identify functional brain networks followed by dual regression to estimate subject-level components for making comparisons of the functional images between the two groups: a group of subjects with Parkinson's disease and a group of healthy control subjects.

We were able to generate subject-level components; however, identifying one component at the group level that included the basal ganglia proved problematic. Methods of identifying neural structures within the application we used provided conflicting evidence. Therefore, we were unable to determine if differences between the study groups existed that could be seen in functional imaging scans.

Testing our primary endpoint using a voxel-wise linear regression with each of the components was not successful because most of the p values on the coefficient of interest were non-significant. In addition, there was a poor model fit seen in the regression models. We were unable to provide scientific evidence of differences that might be seen in functional MRI studies between subjects with Parkinson's disease and healthy control subjects.

Introduction

Parkinson's Disease (PD) is an age-related disorder that affects cognitive and motor abilities and lowers quality of life. As there is currently no cure, it is an area of interest for many research efforts.

Functional MRI (fMRI) is a means of measuring metabolic functioning in the brain. FMRI brain imaging studies have increased markedly in the twenty years since the first study was published (McKeown 1998) in an effort to understand brain disorders.

Brain imaging studies are not used to diagnose Parkinson's disease because it is unclear how it manifests in neuroimages. However, Parkinson's disease has a preclinical phase during which structures within the brain are affected, but external symptoms have not yet manifested (Prodoehl, Burciu, and Vaillancourt 2014). FMRI studies may provide a means of detecting Parkinson's disease during the preclinical phase, possibly allowing earlier intervention.

To analyze the complex data that characterizes fMRI studies, multivariate methods are required. Independent component analysis (ICA) has enabled analysis of fMRI image data by identifying functional brain networks across a study population. Further computations using the estimated components allow comparisons to be made between subjects and across study groups.

In this study, we sought to identify effects of Parkinson's disease that may be seen in functional imaging scans and allow it to be detected earlier in the disease process.

Background

The functioning of the human brain is a compelling and active area of research. As the average lifespan of humans has lengthened, so has the incidence of age-related disorders that affect cognitive and neural processes and lower quality of life. Efforts to

understand the causes and effects of these diseases are the focus of many research studies, which ultimately seek to enhance our understanding of human cognition and brain function.

Parkinson's Disease is a degenerative neural disease with diverse effects, including cognitive and motor symptoms. The course of progression of PD includes a preclinical phase during which structures within the brain are affected, but external symptoms may not have manifested (Prodoehl, Burciu, and Vaillancourt 2014). Researchers and clinicians believe that earlier detection of progressive diseases may help alleviate future suffering and possibly help to identify successful treatments.

Magnetic resonance imaging (MRI), provides high-resolution images of internal structures of the body. Functional MRI (fMRI) is an adaptation that records the presence of oxygen in blood. Oxygenated blood flow increases in response to biological activity; measuring the change in oxygenated blood in neural structures serves as a proxy for measures of metabolic functioning in the brain. FMRI has become popular because it can do this without ionizing radiation, making it safer for patients and more accessible to researchers and clinicians.

Earlier studies using fMRI had subjects perform specific tasks to investigate which parts of the brain became active in response. More recently, there has been an increased interest in "resting state" studies, in which subjects are passive during their scans. These studies show which parts of the brain are active in the absence of outside stimuli. An important finding of this research has been identification of a "default mode network": a network of areas within the brain that operate when other functional areas are not being engaged (Greicius et al. 2003).

Use of resting state fMRI brain imaging has opened up a wide area of research: investigating the ways in which various neurological and psychiatric disorders affect the functional physiology of the brain. Subjects are not required to perform tasks or follow instructions during their scans, which can be a hindrance with many health-related conditions.

Brain imaging studies are not used to diagnose Parkinson's disease because it is unclear how it manifests in neuroimages. At present, patients with suspected Parkinson's disease are only referred for functional imaging studies if needed to rule out other disorders.

In this study, we sought to characterize the effects of Parkinson's disease that can be seen in resting state functional imaging scans. We examined functional brain images of individuals with Parkinson's disease while off medication and compared these images to those of healthy control subjects to investigate whether differences were observed between the groups.

Specifically, we were interested in whether there were particular areas in the brain that showed consistently different levels of functional activation between the study groups and if so, were the images of Parkinson's disease subjects affected by length of time since diagnosis.

To assess differences between groups we used independent component analysis (ICA), which will be discussed in more detail below. Thus a secondary objective of this study was to show how ICA could be used to identify and measure hidden signal sources in fMRI images.

The Study Cohort

We obtained functional MR images from a group of 27 individuals who had been diagnosed with Parkinson's disease while off medication and a healthy control group of 31 subjects. Patient demographics are presented in Table 1. This data was initially collected as part of a larger study whose intent was to compare functional images of a group of individuals with Parkinson's disease while on and while off medication and included a control group.

The study groups were similar in size, but the control group was more heterogeneous. The Parkinson's disease subjects were mostly male (82.5% versus 48.4%, p=0.013) and older than the control group (average age: 64.0 versus 57.8, p=0.024); these differences

were statistically significant. The control group was also more racially diverse: the Parkinson's subjects had only one non-Caucasian (1 person, 3.7%, was Asian) while the control group was 71.0% Caucasian and had individuals of several other races and ethnicities present, p-value across groups=0.035. Both groups were similar with respect to education level and handedness.

Subjects also completed a number of psychometric instruments.

Table 1. Subject demographics

	Parkinson's group n=27	Control subjects n=31	p-value*
Age	64.0	57.8	0.024
Sex (Males)	22 (82.5%)	15 (48.4%)	0.013
Race			
African-American	0	5 (16.1%)	0.035
American Indian	0	1 (3.2%)	
Asian	1 (3.7%)	2 (6.4%)	
Caucasian	26 (96.3%)	22 (71.0%)	
Hispanic Caucasian	0	1 (3.2%)	
Hand dominance (right handed)	23 (85.2%)	28 (90.3%)	0.340
Depression: current	11 (35.4%)	3 (10.0%)	0.223
history	0	3 (10.0%)	
Education–years (mean/SD)	16.3 (2.8)	17.5 (2.2)	0.433
Months since diagnosis (mean/SD)	31.1 (49.0)	--	

* Two-sample t-test or Fisher's exact test

Following is a brief introduction to Parkinson's disease and an overview of the current study. Next is a discussion of functional magnetic resonance imaging (fMRI) and an introduction to resting state studies using fMRI. Finally, we provide an overview and discuss a method that is frequently used to analyze image data: independent component analysis. We describe one method in the context of fMRI functional images and later show ways in which the results can be used to make comparisons between study groups' functional images.

Parkinson's Disease

Parkinson's disease (PD) is a neurological disorder that affects more than one million Americans and ten million individuals worldwide (Tahmasian et al. 2017). It is a progressive disease, although the rate of progression varies by individual.

Parkinson's disease is characterized by loss of motor function and control as well as other neurological effects, such as cognitive impairment, depression, and anxiety (Tahmasian et al. 2017). Symptoms of Parkinson's disease result from a progressive loss of neural cells that transmit dopamine within specific structures in the brain, collectively known as the basal ganglia (see Figure 1).

Figure 1 Structures of the basal ganglia

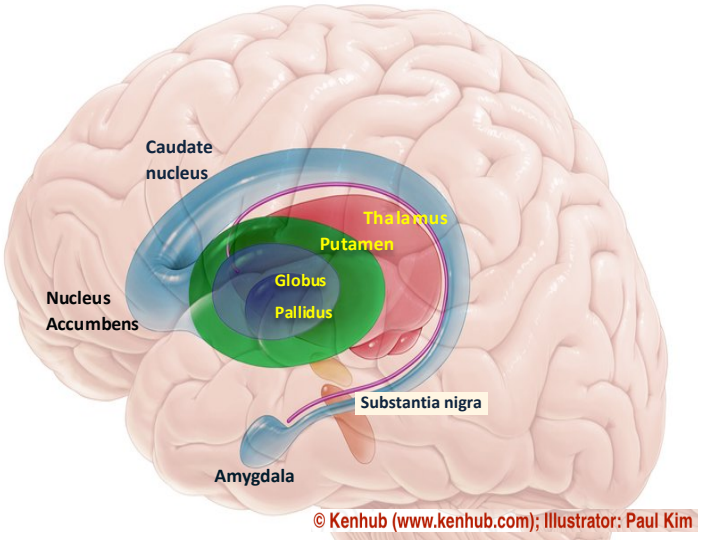

The course of progression of PD includes a preclinical phase during which structures within the brain are affected, but external symptoms are not yet apparent (Prodoehl, Burciu, and Vaillancourt 2014). By the time motor symptoms emerge, an estimated loss of 50% of neurons in the substantia nigra, a structure within the basal ganglia (see Figure 1), has already occurred (Prodoehl, Burciu, and Vaillancourt 2014). The substantia nigra is the principal source of dopamine for other structures in the basal ganglia.

The symptoms of Parkinson's disease are well known, but much is still unknown: there are no clear causes, although the risk increases with age and there is believed to be a genetic component. There is no conclusive indicator of Parkinson's disease nor is there a definitive means of diagnosing it, although symptom improvement with dopamine replacement medication is highly suggestive (Mayo Foundation for Medical Education and Research 2018).

Functional Imaging

Functional MRI (fMRI) uses the MRI's magnetic field to stimulate hemoglobin, allowing it to measure the presence of oxygen in blood. Oxygenated blood flow increases in tissues that require increased fuel needs for biological activity; thus the change in oxygenated blood in neural structures serves as a proxy for metabolic functioning in the brain.

Functional image data are a series of signal activations that are sampled from discrete locations across subjects' brains over a course of time. Coordinated fluctuations of activations from spatially separated areas of the brain suggest functionally coherent neural connections (Li et al. 2009). These functionally connected areas are referred to as sources; each source represents an independent neural system that produces activation signals when it is functioning. Figure 2 shows an illustration of four independent sources and the resulting mixed signals that is recorded during the fMRI scanning session. Appendix A shows a collection of source network maps that were identified in populations of subjects by one researcher during fMRI resting state studies using ICA (Shirer et al. 2012).

Figure 2 Schematic of four independent sources

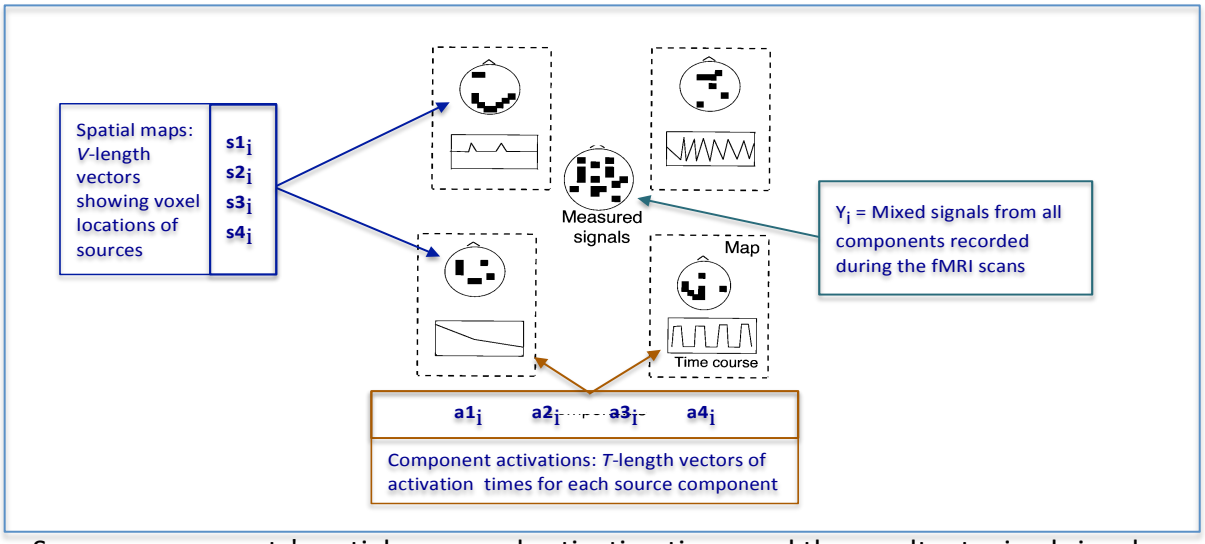

Source components' spatial maps and activation times and the resultant mixed signals captured during an fMRI scan (Orig. source: McKeown et al. Human Brain Mapping, 1998.

Spatially, the MRI scanner samples signals in a regular 3-D grid of cubic volumes that circumscribe subjects' brains. In this study, each voxel measurement encompassed an 8 mm^3 cubic volume. Data is mapped onto point volumes known as "voxels." A contraction of "volume" and "elements," it is the three-dimensional equivalent of a pixel. Voxel locations are determined by the scanning equipment independently of the anatomy of subjects' brains. A visual representation of the path of the data is shown in Figure 3 and is described in greater detail below.

Temporally, data are a series of measures taken successively, typically for several minutes. The time between scans is a function of the equipment and the study parameters determined by the researcher. Although there is a temporal component to the data, electric signals pass quickly through the brain (on the order of nanoseconds) (Parizh 2002) while each full-brain image takes several seconds to capture. In this study, whole-brain scans were taken every five seconds. Changes in signal intensity levels throughout the brain occur at far higher frequencies than the scanning equipment can capture. The model used in independent component analysis does not make use of any temporal correlations that may be present (Hyvärinen and Oja 2000).

Within a voxel-sized volume of the brain, there can be up to one million neurons. Measured activation levels at each voxel may be a direct measure of the signal from one source or from a combination of overlapping disjoint sources. Analytic methods that are able to take into account such unknown data dependency are advantageous.

Separation of the fMRI signals into distinct temporally correlated brain activations enables inferences to be made about networks of signals. This problem is similar to one seen in the signal processing literature called blind source separation. One method used to address this is independent component analysis, which identifies a collection of independent signal sources from samples recorded at multiple locations. The first application of independent component analysis to fMRI data was done by McKeown et al. (1998). Since then, it has become a frequently used method throughout the fMRI literature.

Performing independent component analysis (ICA) with data from all subjects allows "large-scale patterns of functional connectivity" common to a majority of subjects to be identified (Beckmann et al. 2009). Data from the entire study group are combined to identify functionally coherent areas of the brain present among the majority of subjects i.e., common sources of functional activation across the study population. Its fundamentals are described below. After performing independent component analysis, further processing of the data must be done to enable analyses at the subject and group levels. This is discussed in later sections.

Resting State Functional Imaging Studies

In many studies in which fMRI is used, subjects are asked to perform specific tasks, allowing the underlying neural processes to be identified. In resting state studies, subjects are not asked to perform experimental activities; their purpose is to record the brain activity of individuals at rest to identify neural processes that are operative in the absence of external stimuli.

Brain imaging data can identify sources of signal activations with common spatial mappings throughout the study population. In addition, functional brain networks are sets of brain regions showing temporal coherence with one another (Calhoun 2012).

Independent Component Analysis

Fundamentals

The underlying model is represented by **J**=**AS**, where **J** are observed measures of signal activations captured during an individual's brain scanning session over time. **S** are spatial mappings of individual sources and **A** is an invertible mixing matrix that maps the activations of the source networks over time to yield the observed data.

Although the data is recorded in three-dimensional space, it is converted to a vector and conditioned to facilitate the analysis. The transformations of the data from collection up to the independent component estimation is described below and shown in Figure 3.

One functional image is $\mathbf{Y}_i(t)$, a V–length row vector of signal activation measures collected from all V possibly-active voxels at time t for subject i. The dataset $\mathbf{Y}_i$ is a $T \times V$ matrix of T images captured at T time points for subject i. Refer to Figure 3 for a graphic representation of this and the successive discussion.

Figure 3 Data Flow Illustration

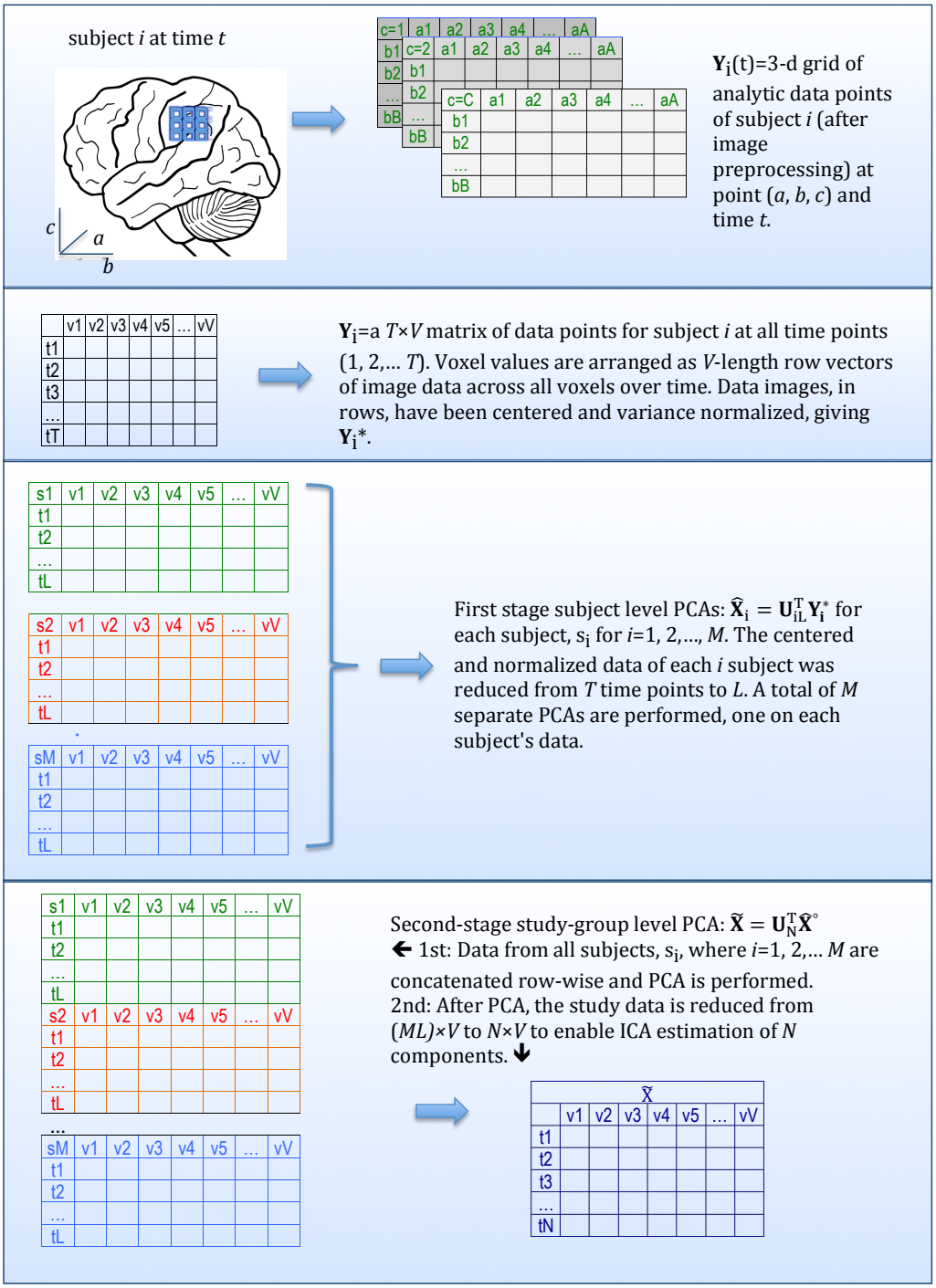

In this study, each subject's original dataset was a four-dimensional matrix of signal activation levels sampled at 8 mm^3 volumes within a 91×109×91 grid. Although this represents a collection of 902,629 points in space, the number of points that contained

subjects' data was a much smaller set: there were V=190,446 points identified by the MRI scanner's system software as active voxels. Along the fourth dimension, each subject had T=94 recorded images, captured every 5 seconds. The four-dimensional dataset was converted to a two-dimensional $T \times V$ matrix, $\mathbf{Y_i}$.

The number of sources, N, is an *a priori* assumption that must be determined by the researcher before independent component analysis can be performed. The number of assumed sources can be any number less than or equal to the number of samples per observation—in this study it was 94, the number of time points. We chose N to be 20, using heuristics based on prior research (Chou, 2018).

Without *a priori* assumptions available, the number of components can be determined using information theoretic measures. Three commonly used measures are Akaike's Information Criteria (AIC), Bayesian Information Criteria (BIC), and Minimum Distance Length (MDL). Refer to Cichocki 2014; Hyvärinen, Karhunen, and Oja 2001; or Li, Y., Adalı, and Calhoun 2007 for more details.

If there are assumed to be fewer sources than samples (which is usually the case) the data must be preprocessed to reduce the number of samples (in this study, time points, T=94) to N, the number of assumed sources. Analytic preprocessing using principal component analysis (PCA) is used to transform the study data by reducing it from $(MT) \times V$ (58×94×190,446) to (ultimately) $N \times V$ (20×190,446), where M=58 is the total number of subjects and N, T, and V are as above.

Independent component analysis identifies individual sources (i.e., components) by seeking sources with higher-order statistical independence. The objective is to estimate the $N \times N$ unmixing matrix $\mathbf{W}=\mathbf{A}^{-1}$ with weights that generate maximally independent source vectors. Spatial ICA separates a matrix of fMRI data into components representing independent patterns of activity described by spatial maps and a corresponding set of fMRI activation time courses (McKeown et al. 1998).

For independent component analysis, the independent component model of the data assumes the N random variables, y_j where $j = 1,\ldots,N$ are modeled as linear combinations of a mixture of N sources, s_j as $y_j = a_{j1}s_1 + \ldots + a_{jN}s_N$ where the a_j**.** are from a square, invertible matrix A, which is to be estimated.

The s_j are latent, they are not observed, so the model has infinitely many solutions: if $y_j = \sum_{j=1}^{N} a_j s_j$ is a solution, so is $y_j = \sum_{j=1}^{N} \frac{1}{\beta_j} a_j (\beta_j s_j)$. To limit the space of possible solutions, we make the simplifying assumption that the sources have unit variance: $E[s_j^2]=1$. There is still ambiguity related to the sign of the solution, but this is generally considered ignorable.

Although the underlying model has a linear form, as does the model used in ordinary least-squares regression (OLS), OLS can be solved analytically because both the independent and the dependent variables are known; estimating the parameters requires a matrix inversion (e.g., finding the pseudoinverse of the design matrix). With independent component analysis, only the dependent variables are observed. Since they are assumed to represent a linear mixture of the model parameters, **A**, and the sources, **S**, neither of which are known, an analytic solution cannot be found. Both sets of values must be estimated simultaneously (Hyvärinen, Karhunen, and Oja 2001).

"Independent component analysis" is actually not a single method, but a family of over 30 methods. Each is distinguished by two characteristics. The first is the contrast (also called an "objective," "cost," or "score") function used to evaluate the amount of independence achieved among components during the optimization procedure. Estimates are determined iteratively starting with the observed data and a matrix of arbitrary values.

Second is the optimization method used to update the estimates after each iteration (Hyvärinen, Karhunen, and Oja 2001; Comon 1994) until the independence of components is maximized.

Three methods that are frequently used for fMRI analysis are the following (Jenkinson et al. 2012; Calhoun, and Adali 2012; Smith 2004):

JADE (joint approximate diagonalization of eigenmatrices—uses cumulants and gradient descent (Jacobi technique);

Infomax—uses entropy to maximize information transfer with a gradient descent algorithm;

FastICA—uses negentropy as an estimate of independence approximated by non-Gaussianity, and fixed point iteration.

A study that compared these three algorithms found that all were reliable and led to consistent estimates after repeated runs with random starting values and input parameters (Correa, Adalı, and Calhoun 2007). The discussion that follows primarily focuses on FastICA, which will be described in more depth in a later section.

Typical implementations of FastICA (Hyvarinen 1997; Hyvärinen, Karhunen, and Oja 2001) and Infomax (McKeown et al. 1998) assume the signals of interest are super-Gaussian random variables (see Figure 4 for an example); any sub-Gaussian components are more likely to be noise. Signals occur within a narrow frequency band and noise is more diffuse. A clear signal has the majority of its data occurring close to the mean frequency and scattered noise-related signals occur far less often at frequencies further from the mean. The super-Gaussian assumption is therefore appropriate for this application of ICA.

Figure 4. Example of a super-Gaussian distribution

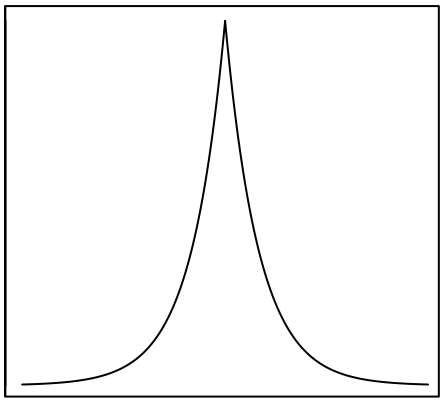

Laplace(μ,B=0.5)

Before analysis is possible, data collected from the MRI scanner after each subject's scan session must be preprocessed to address issues that are inherent in raw functional MRI data and would otherwise preclude comparative analyses. These are described below; however, this study analyzed images that had already undergone such pre-processing, so the following are for descriptive purposes only.

Preprocessing

Preprocessing corrects for sources of noise and artifact and provides a common point of reference in time and space to enable comparisons between subjects (Cole, Smith, and Beckmann 2010). Some of the preprocessing steps taken will depend on the type of analysis being considered; these are the preprocessing steps that were performed on the data used in this study [Chou 2019]:

Motion Correction—This helps to ensure anatomical coordinates are consistent between successive scans of each subject. While this is always necessary it is not sufficient to remove motion-related noise in the data.

Brain extraction—Removes scan data collected from non-brain regions (e.g., the skull) to help with the registration process and to limit the computational load to only relevant data points. A mask defining the active data region can be defined by either the scanner system software or by the fMRI analysis software.

Slice Timing—Corrects for the manner in which data is captured by the scanner: one complete image is captured in two successive passes of the MRI scanner detectors. The MRI system synchronizes these measures into a single image.

Spatial Smoothing—Used to improve the signal-to-noise ratio; data across a continuous volume is measured at discrete points in space and may be subject to sampling error. To improve consistency between measures at adjacent voxels a Gaussian kernel-based smoothing function is used. This helps to compensate for information lost due to sampling, improve consistency within and between subjects, and better condition data

for Gaussian random field theory assumptions, which is used to control family-wise error rates (Wager 2009). The kernel size is determined by image characteristics. This can help improve image resolution and differentiate overlapping signals.

Registration—functional images are overlaid onto a structural image from each subject and then transformed to fit onto a standard brain template to enable comparisons between individuals. The template used in this study (and many others) was the MNI-152 (Jenkinson and Smith 2001).

Band-pass filtering—signals are frequently filtered to increase the signal to noise ratio and improve the component estimation. Signals of interest are in the range of 0.01 to 0.10 Hertz.

After the above preprocessing, principal component analysis is performed on each subject's data to reduce its dimension and remove second-order linear dependencies within (i.e., decorrelate) it. Each image is a V-length row vector of signal activation measures across all V active voxels. Each subject's data is a collection of T image vectors, i.e., a $T \times V$ matrix of images over time, designated here as $\mathbf{Y_i}$, a set of images for subject i.

The images (rows) of the $T \times V$ matrix are mean-centered and variance normalized, giving $\mathbf{Y}_i^*$. PCA is then used to both reduce the dimensionality of the data and to whiten it. This is also referred to as "sphering," as it represents the basis vectors in a multi-dimensional unit sphere. The resulting data matrix is orthogonal.

We used singular value decomposition (SVD) to generate the eigenvectors of $\mathbf{Y_i}^*$. SVD translates any matrix, in this case a $T \times V$ matrix, into three matrices: a $T \times T$ left unit-length orthogonal eigen-matrix, $\mathbf{U}$; a $V \times V$ right unit-length orthogonal eigen-matrix, $\mathbf{V}$; and a $T \times V$ matrix, $\mathbf{\Sigma}$, that has the corresponding singular values along the main diagonal with zeroes in off-diagonal positions.

If the values of $\mathbf{\Sigma}$ are in descending order, the data reduction and whitening transformation takes the corresponding L columns of $\mathbf{U}$, $\mathbf{U}_{\mathrm{L}}$ to transform $\mathbf{Y}_{\mathrm{i}}{}^{*}$. For subject i this yields

$$\widehat{\boldsymbol{X}}_{\mathrm{i}} = \mathbf{U}_{\mathrm{i}\mathrm{L}}{}^{\mathrm{T}}\mathbf{Y}_{\mathrm{i}}{}^{*},$$

where $\widehat{\mathbf{X}}_i$ is the resulting $L \times V$ reduced-dimension data matrix.

The first-stage principal component analysis is repeated M times, once with each subject's data. The columns of $\widehat{\mathbf{X}}_i$ are normalized by dividing by their standard deviations, which gives $\widehat{\mathbf{X}}_{\mathrm{i}}^{\circ}$.

After each subject's data has been reduced and whitened by PCA, the image data from all M subjects are concatenated row-wise, giving a $(ML) \times V$ matrix:

$$\widehat{\boldsymbol{X}}^{\circ} = \begin{bmatrix} \widehat{\boldsymbol{X}}_1^{\circ} \\ \vdots \\ \widehat{\boldsymbol{X}}_M^{\circ} \end{bmatrix}$$

where $\widehat{\boldsymbol{X}}_{\mathrm{i}}^{\circ}$ are $L \times V$ matrices for subjects i=1, 2,…M.

After the first-stage PCAs, the subject-level datasets, now in a single matrix, $\widehat{\mathbf{X}}^{\circ}$, are reduced again in the second stage PCA, which reduces the number of time points from ML to the appropriate size for the independent component analysis, i.e., N. The SVD of the concatenated data of all M subjects yields

$$\widetilde{\mathbf{X}} = \mathbf{U}_{\mathrm{N}}^{\mathrm{T}}\widehat{\mathbf{X}}^{\circ}$$

where U_{N} are the N left leading eigenvectors of $\widehat{\mathbf{X}}^{\circ}$. The final analytic data matrix, $\widetilde{\mathrm{X}}$, is $N \times V$, where N is the number of independent components to be estimated and V is as above.

Independent component analysis can then be used on the final reduced dataset, $\widetilde{\mathbf{X}}$, to estimate the spatial maps of the source components and an invertible $N \times N$ mixing matrix, **A**, where

$$\widetilde{\mathbf{X}} = \mathbf{AS}$$

and the N rows of the estimated matrix, **S**, are the spatial maps that describe the voxel locations of each of the N estimated source components and **A** corresponds to a $N \times N$ mixing matrix that maps the group-level sources onto the reduced subject data.

Independent component analysis relies on the assumption that the N estimated sources in **S** are statistically independent (Calhoun, V. D. et al. 2001; Hyvärinen, Karhunen, and Oja 2001). A consequence of the Central Limit Theorem is that the distribution of a sum of independent non-Gaussian random variables or vectors is closer to Gaussian than any of its constituents. To find statistically independent components, we look for components that are maximally non-Gaussian. The way this is determined is discussed below.

The goal of independent component analysis is to find a weight matrix, **W**, that maps the conditioned data onto a set of (unknown) statistically independent source component vectors, $\mathbf{S}=\mathbf{W}\tilde{\mathbf{X}}$. Having the conditioned, observed data $\tilde{\mathbf{X}}$, we need to identify an invertible matrix **W,** with $\mathbf{W}^{-1}=\mathbf{A}$, that defines a linear transformation mapping the source components onto the conditioned data, $\tilde{\mathbf{X}}=\mathbf{W}^{-1}\mathbf{S}=\mathbf{AS}$. Independent component analysis seeks to find a set of weight vectors, $\mathbf{w}_j$, where $j=1, 2,\ldots.N$, the number of components, to maximize the non-Gaussianity of $\mathbf{W}\tilde{\mathbf{X}}$.

Figure 5 Schematic of ICA

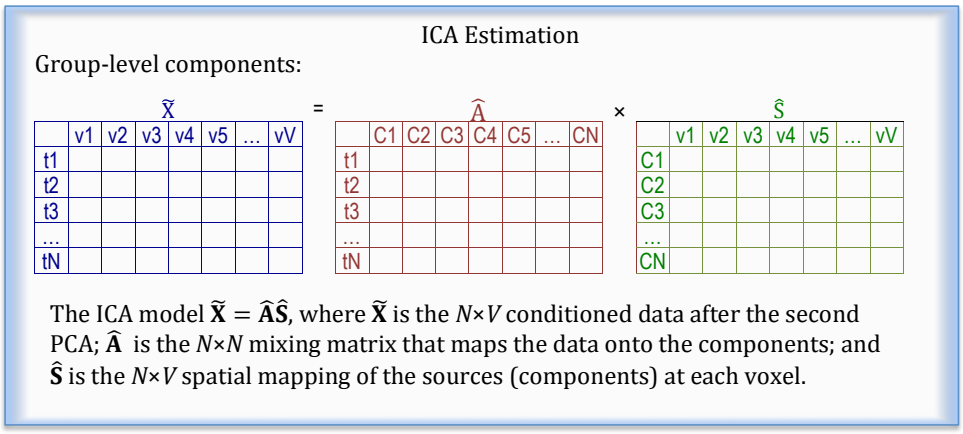

FastICA

For FastICA, Hyvärinen, the creator of FastICA, chose to use a contrast based on an approximation of negentropy, a measure used in Information Theory. Entropy is a measure of randomness in a random variable. Variables with greater randomness (higher entropy) contain less information; Gaussian variables have the highest entropy of all random variables with a given variance.

Negentropy is a measure of the difference in entropy between a random variable and a Gaussian random variable with equal variance. Maximizing negentropy of an estimated component finds components with the lowest entropy and enforces maximum independence.

Negentropy can be approximated by: $J(y) \propto [\mathrm{E}\{H(y)\} - \mathrm{E}\{H(v)\}]^2$ where y and v have the same mean and variance and $v \sim \mathrm{N}(0,1)$—is a standard normal (i.e., Gaussian) random variable. H, the contrast function, is an arbitrary user-defined nonlinear twice-differentiable function (Hyvärinen, Karhunen, and Oja 2001).

Hyvärinen has done extensive testing on different contrast functions and optimization algorithms. He provides three options for contrast functions that have been shown to have desirable statistical properties such as consistency and reasonably fast convergence (Hyvärinen, Karhunen, and Oja 2001; Hyvärinen 1997; Hyvärinen 1999):

1. $H_1(u) = \frac{1}{a}\log\cosh(au)$ with $H'_1(u) = \tanh(au)$ and $H''_1(u) = (1 - \tanh^2(au))$, where 1≤a≤2 (often a=1*), which was found to be a "good general-purpose contrast function" and a robust estimator.
2. $H_2(u) = -e^{\left(-\frac{u^2}{2}\right)}$ with $H'_2(u) = ue^{\left(-\frac{u^2}{2}\right)}$ and $H''_2(u) = (1 - u^2)e^{\left(-\frac{u^2}{2}\right)}$, which is better if components are highly super-Gaussian; it was found to be more robust than the others and may be more computationally efficient, if performance is of concern.
3. $H_3(u) = \left(\frac{1}{4}\right)u^4$ with $H'_3(u) = u^3$ and $H''_3(u) = 3u^2$, which is related to the use of kurtosis as one of the first measures of Gaussianity used in ICA; as a quadratic equation it is conceptually simple and was easy to program when computation speed was an issue, but it is also sensitive to outliers; Hyvärinen states that this is better when sub-Gaussian components are expected.

The FastICA Algorithm

Hyvärinen describes his fixed-point ICA algorithm, which he named FastICA, in the following manner (for the derivation see Appendix E) (Hyvärinen, Karhunen, and Oja 2001):

1. Start with the conditioned $N \times V$ data matrix and
2. Choose an initial $N \times 1$ normed vector $\mathbf{w}$ (the initial values are arbitrary; many algorithms use a vector of randomly generated values)
3. While P<N, calculate the Pth column of $\mathbf{W}$, w_P, until convergence is reached:

$$\mathbf{w}_P = \frac{\left[\tilde{\mathbf{X}}\mathrm{H}\left(\mathbf{w}^T\tilde{\mathbf{X}}\right)\right] - \left[\mathrm{H}'\left(\mathbf{w}^T\tilde{\mathbf{X}}\right)\right]\mathbf{w}}{V}$$

   which produces a $N \times 1$ vector
4. Renormalize with $\mathbf{w} = \frac{\mathbf{w}_P}{\|\mathbf{w}_P\|}$
5. Repeat steps 3 and 4 until converged.

This algorithm identifies components sequentially; to prevent the algorithm from converging to the same maxima multiple times, the outputs $\mathbf{w}_i{}^T\mathbf{x}$ should be decorrelated after every iteration by subtracting a projection of the prior components

*Hyvärinen does not specify when a value of a>1 might be preferable.

from the newest component: $\mathbf{w}_\mathrm{p} = \mathbf{w}_\mathrm{p} - \sum_{\mathrm{k}=1}^{\mathrm{p}-1} \mathbf{w_k} \mathbf{w_p^T} \mathbf{w_k}$ and then renormalizing $\mathbf{w}_\mathrm{p} = \frac{\mathbf{w_p}}{\|\mathbf{w}_\mathrm{p}\|}$.

When all *N* vectors of $\mathbf{w}$ have been estimated, concatenate them into the columns of $\mathbf{W}$ and calculate the source vectors as $\hat{\mathbf{S}}$=$\mathbf{W}\tilde{\mathbf{X}}$.

Analysis of Components

After the independent component analysis is performed, the estimated set of components, $\widehat{\boldsymbol{S}}$, is an *N*×*V* matrix of the *N*=20 components. Each row of $\widehat{\boldsymbol{S}}$ describes a source component's spatial mapping, i.e., its location among the *V*=190,446 voxels in the "group-averaged" study subject's brain.

These components were estimated using the data from the entire study population and represent a composite image averaged across the entire study group. It is not possible to draw inferences at the subject-level or to make comparisons across subgroups. To enable this, further procedures must be performed to generate subject-specific component estimates. Two principal methods are used to do this: back reconstruction (Calhoun, V. D. et al. 2001; Erhardt et al. 2011) and dual regression (Beckmann et al. 2009; Smith et al. 2009).

Back reconstruction takes each component and for each subject reverses the transformations performed during the two PCA procedures. It essentially reverses the conditioning steps used to prepare each subject's image data for independent component analysis.

Dual regression, which is used here, uses a two-step least-squares approach to estimate components for each subject. Also refer to Figure 6. The first step estimates the time course of activation for each component. The equation is

$$\mathbf{Y}_\mathrm{i} = \mathbf{A}_\mathrm{i}^{+} \hat{\mathbf{S}} + \mathbf{E}_{1\mathrm{i}}$$

where $\mathbf{Y}_\mathrm{i}$ is the subject's observed data, prior to the PCA data reductions, $\hat{\mathbf{S}}$ are the estimated components, common to all subjects, and $\mathbf{A}_\mathrm{i}^{+}$ are time course activations of

each component for each subject to be estimated, plus an error term with $E[\mathbf{E}_{1i}]=0$. We use this notation for clarity, to remain consistent with the model notation; however, the "+" is used to signify that $\mathbf{A}$ is no longer an $N \times N$ mixing matrix, but contains as many time points as the subject's original data. $\mathbf{A}_i^+$ is $T \times N$, giving the activation levels of each subject's components over $T=94$ time points for the $N=20$ components.

The OLS estimate of $\mathbf{A}_i^+$, the subject-specific time course is then

$$\widehat{\mathbf{A}}_i^+ = \mathbf{Y_i}\,\hat{\mathbf{S}}^T\left(\hat{\mathbf{S}}\hat{\mathbf{S}}^T\right)^{-1},$$

where $\mathbf{Y_i}$ is the subject's observed data, prior to the PCA data reductions. The second step of the dual regression uses $\widehat{\mathbf{A}}_i^+$, the subject-specific time courses from the first step, and relaxes the assumption of a common spatial mapping of the sources across all subjects to identify subject-specific spatial mappings corresponding to the full time course associated with each component:

$$\mathbf{Y_i} = \widehat{\mathbf{A}}_i^+ \mathbf{S}_i + \mathbf{E}_{2i}\,,$$

where $\widehat{\mathbf{A}}_i^+$ are the subject-specific time courses estimated in Step 1, $\mathbf{S_i}$ are spatial mappings of the sources for each subject to be estimated, plus an error term with $E[\mathbf{E}_{2i}]=0$. The estimated $\hat{\mathbf{S}}_i$, are

$$\hat{\mathbf{S}}_i = \left(\widehat{\mathbf{A}}_i^{+T}\widehat{\mathbf{A}}_i^+\right)^{-1}\widehat{\mathbf{A}}_i^{+T}\,\mathbf{Y_i}.$$

Figure 6 Dual regression

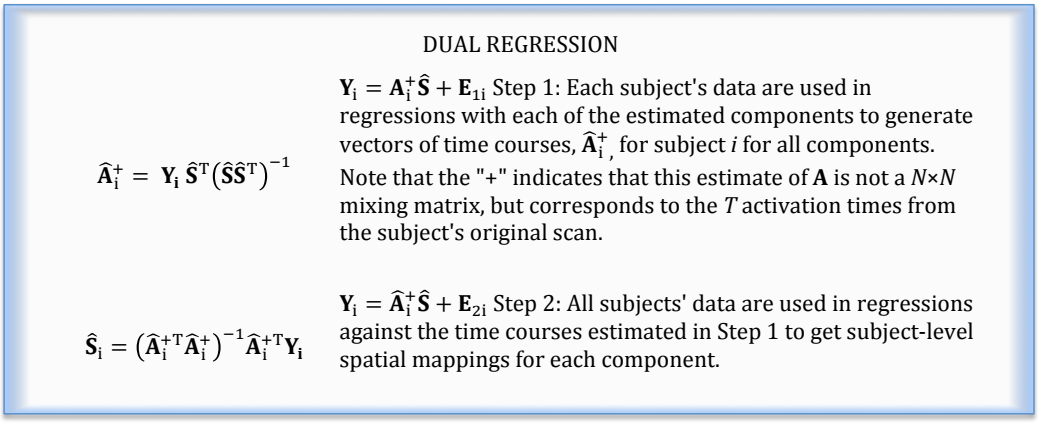

While the assumptions seem contradictory (i.e., the common spatial mappings can reveal subject-specific time courses, which in turn can identify subject-specific spatial mappings) according to Calhoun & Adali, in practice the method seems to work "quite well" (Calhoun, Vince D. and Adali 2012). The dual regression procedure yields a total of *NM*=1160 component image and time course pairs, $\{\hat{\mathbf{s}}^{\mathbf{T}}_{ij}, \hat{\mathbf{a}}_{ij}{}^{+}\}$, where *i*=1, 2, …, 58 and *j*=1, 2, …, 20, identifying a set of *N*=20 components for each of the *M*=58 study subjects.

The end result for each subject was a set of *N*=20 component vector pairs consisting of the spatial maps, $\hat{\mathbf{s}}_{ij}$, each of which is a vector with *V*=190,446 elements that identified the voxels in which the component was present, and $\hat{\mathbf{a}}_{ij}{}^{+}$, a *T*=94-element vector that contains the timeline of activations of that component. Note that $\hat{\mathbf{a}}_{ij}{}^{+}$is the *j*th column of $\hat{\mathbf{A}}_i{}^{+}$ and $\hat{\mathbf{s}}_{ij}$ is the *j*th row of $\hat{\mathbf{S}}_i$.

After the subject-level component spatial maps and time courses are estimated, the time courses for the *N* group-level components are estimated using an average of all *M* of the subject-level time courses for that component. For each *j*=1, 2, …, 20 component, the average time course is $\hat{\mathbf{a}}_j^+ = \frac{\sum_{i=1}^{M} \hat{a}_{ij}^+}{M}$.

Each of the *N* group-level component pairs, $\hat{\mathbf{a}}_j{}^{+}$ and $\hat{\mathbf{s}}_j$ where j=1, 2, …*N* and the *NM* subject-level component pairs: $\hat{\mathbf{a}}_{ij}{}^{+}$ and $\hat{\mathbf{s}}_{ij}$, where i=1, 2, …, *M* and j is as above,

respectively, consists of the spatial map $\hat{\mathbf{s}}$, which is a *V*-length row vector identifying the voxels where each component is located within the brain and a *T*-length column vector, $\hat{\mathbf{a}}^{+}$ indicating the times at which that component was active over the course of an "average" scanning session.

Each component is stationary: the voxel-level spatial mapping of components (those at both the subject-level, $\hat{\mathbf{s}}_{ij}$, and the group level, $\hat{\mathbf{s}}_{j}$,) is fixed for that component, i.e., components do not change over time. Similarly, the time course of activation (at both subject level, $\hat{\mathbf{a}}_{ij}^{+}$, and group level, $\hat{\mathbf{a}}_{j}^{+}$) applies to all of the voxels within a component simultaneously. The relative activation levels between voxels within a component do not change over time.

Two issues worth noting are related to the values of the data. First, all 20 components had the same number of non-zero voxels—none of the 190,446 voxels in the "active" region of the spatial maps were exactly equal to 0. The components varied in size (i.e., the volume of truly activated voxels), but even the components with the greatest number of active voxels were greater than 4,000 voxels in size.† Thus the majority of the voxels in each component had non-zero values that were not related to actual signal activation. This is presumably due, in part, to artifacts created during image preprocessing procedures and rounding error during the independent component analysis estimation procedure.

This indicated that there was not a clear distinction between "activated" and "non-activated" voxels; they were not strictly "on" or "off." The threshold for what is considered an "activated" voxel should be determined before the analysis. Investigators

---

† Data not presented; detailed data on components, including locations within the brain and the volume of each component within each location were produced by the GIFT application. The largest component measured approximately 30 cc (30,000 mm^3 or 3,750 voxels).

typically choose a threshold value based on t or z scores, where the null hypothesis is zero activation. In this study, we chose to use a t score threshold arbitrarily set at 2.0.

Second, the voxel activation levels can be negative, which would indicate a waning of oxygenated blood levels in that area. However, some investigators choose to disregard negative values, given that their interpretation may be a little ambiguous—the amount of oxygenated blood decreases after neural activity has ceased, but it may also decrease if the oxygenated blood was detected in an area where it had been stored, on reserve, until needed by other nearby neural structures. Areas in which this occurred would likely appear as speckled on fMRI images, with areas of positive and negative activation in close proximity. The component images displayed in this study were limited to include only positive voxel values.

Methods

Using data from 58 individuals, 27 with Parkinson's disease and 31 controls, we extracted 20 independent components (i.e., 20 group-level pairs) using FastICA (Hyvärinen, 2001). After preliminary examination of the group-level components, described next, dual regression was used to generate subject-level components for the primary analysis and group-level comparisons.

The primary software application used was Group ICA/IVA of fMRI Toolbox (GIFT), which was developed by Calhoun & Rachakonda (2018). Additional computation was performed using R statistical programming software version 3.4.4 (R Core Team 2018) and the oro.nifti package, version 0.9.1 (Whitcher, Schmid, and Thornton 2011).

Group-level Components

Spatial maps of $\hat{\mathbf{s}}_j$, the group-level components (shown in Appendix B) were first examined individually to see which showed evidence of patient movement or other signs of noise-related signals and which appeared to represent viable activation sources (Griffanti 2015). Evidence of noise was noted, but none of the components were removed from the rest of the analysis.

While the theory behind them is beyond the scope of this thesis, power spectra of the group components are also important to consider so were included in the components overview. Power is the inverse of signal activation frequency and is calculated from time-sampled signals using a discrete time Fourier transformation.

While frequency is measured in cycles per second; the power is its inverse as a measure average frequencies across time. In essence, spectral plots are histograms of signal activation frequency levels.

In an ideal signal, the power spectra would show a high peak of activation at the mean frequency and fewer activations at other frequencies, i.e., would be super-Gaussian. It is this characteristic that enables the ICA algorithm to identify source components. Some

results from the power spectra plots are discussed below; plots for all components are included with the component images in Appendix B.

Region of Interest Analyses

Region of interest (ROI) templates can be used to identify various neural structures or functional networks of interest so they can be located in relation to the components. These templates, which are used by image data processing applications, identify the voxels in which specific structures in the brain are located, so they can be compared to the spatial maps of the components, $\hat{\mathbf{s}}_j$. The GIFT application has several functions that are able to use ROI templates.

Parkinson's disease is known to destroy structures within the basal ganglia, so we wanted to determine which component(s) captured signal activation in these structures. For a labeled illustration of the basal ganglia, refer to Figure 1; for an example of a basal ganglia ROI template within a MRI image, see Figure 7.

Figure 7 Example basal ganglia template from Stanford's atlas

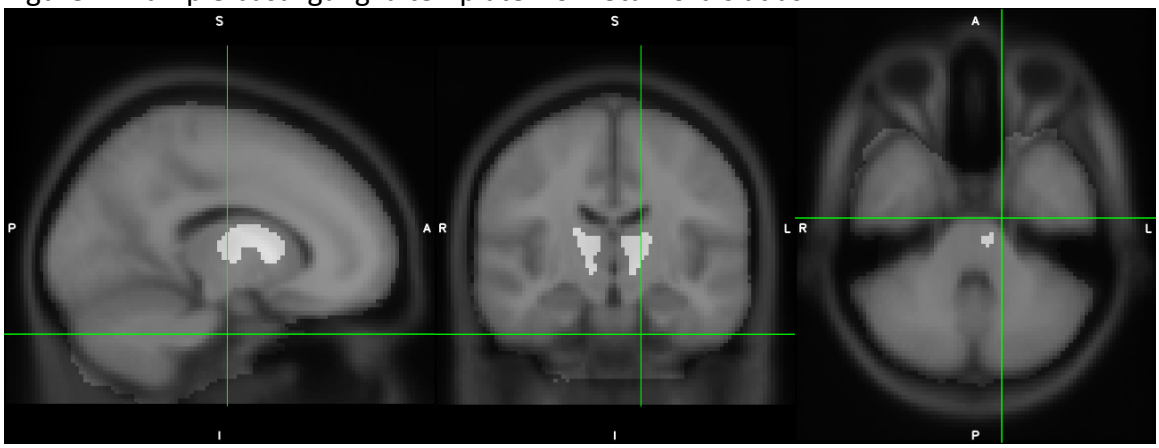

The basal ganglia is the brighter patch near the centers of all three images above. (The green crosshairs frame it in the *x* and *y* coordinates, but point to an area below it in the *z* plane.)

Subject-level Components

After dual regression was used to estimate the subject-level components, $\hat{\mathbf{s}}_{ij}$, and time courses, $\hat{\mathbf{a}}_{ij}{}^{+}$, (i=1, 2, …, *M* and j=1, 2, …, *N)*, the subjects' data were combined by

component to answer the primary research question. Each of the 20 components had M=58 subject-level component vector pairs: $\cup_{\mathbf{i=1}}^{\boldsymbol{M}}\{\hat{\mathbf{s}}_{ij}, \hat{\mathbf{a}}_{ij}^{+}\}$, and a group level vector pair, $\{\hat{\mathbf{s}}_j, \hat{\mathbf{a}}_j^{+}\}$ associated with it.

Histograms of the component activation data were initially plotted by group for each component to look for any notable qualitative differences between groups. This is not a formal statistical test, but provides a quick means of assessing whether any components warrant further investigation because they suggest there may be differences between the groups. The data within each component are from the spatial maps and are a combination of the activation levels of the voxels within each component and the numbers of activated voxels. More-activated voxels will have higher activation levels and larger components will have more activated voxels.

The histograms show the density of the activated voxels in each component, so the histograms can be used to examine the highest activation levels of the voxels within each component, but not the overall size, i.e., number of activated voxels, within each component.

To address the study question of interest, we performed voxel-wise linear regressions across each of the 190,446 active voxels in each component. The regression equation used was designed to test whether the activation level of each voxel was significantly different between study groups, after adjusting for sex and age. In addition, to determine if there was a progressive effect, we used the length of time that had passed since the Parkinson's disease diagnosis was first made to serve as a proxy for the disease severity level in the Parkinson's subjects. The regression models were fitted using the following equation:

$$\hat{\mathbf{s}}_j(k)=\{\text{Months since diagnosis}\}+\text{Sex}+\text{Age}+\epsilon$$

for each component, indexed by j, and where k=1, 2, …, 190,446, giving $\hat{s}_j(k)$ as the kth active voxel for component j.

After each regression model was fitted, we recorded the p-value of the voxel's coefficient to create a "p value map" of a model brain for each component. The resulting brain map would show the voxels significantly affected by the disease longevity, in months since diagnosis. (This would yield a component image, like those seen in the above figures where instead of seeing a map of activation levels, it would show a mapping of the voxels that had statistically significant coefficients in that voxel's respective regression model.)

Results

Specific findings and examples of images are presented and discussed below; for a summary table of findings by component refer to Appendix D.

Figures below include images that are the spatial mappings, the vectors $\hat{\mathbf{s}}_j$, defined by the independent component analysis procedure that have been reassembled into their three-dimensional forms and plotted on "standard" MRI structural images for reference. The MRI images appear in gray scale, the source components are in the red-yellow color scale.

The plots of power spectra shown are based on Fourier transformations of the discrete time-sampled vectors, $\hat{\mathbf{a}}_j^+$. All 20 group-level component images and their associated plots are presented in Appendix B.

Group-level Results—Overview

There were N=20 components, $\hat{\mathbf{s}}_j$ (j=1, 2, …,20), estimated during the independent component analysis procedure. Components 1 and 3 were noted as likely being noise-related (see Figure 8 and Figure 9). Both components show activated voxels that partially encircle the brain, which is typically a result of patient movement and not true functional activation. Figure 8 shows Component 1; the red and yellow squares (two-dimensional images of voxels) show the spatial mapping of the active voxels in this component. The side view on the left and the overhead view on the right show an arc of activated voxels that partially encircles the brain. True activations of signal sources typically appear in clumps in one or more confined areas.

Figure 8 Three orthographic views of Component 1

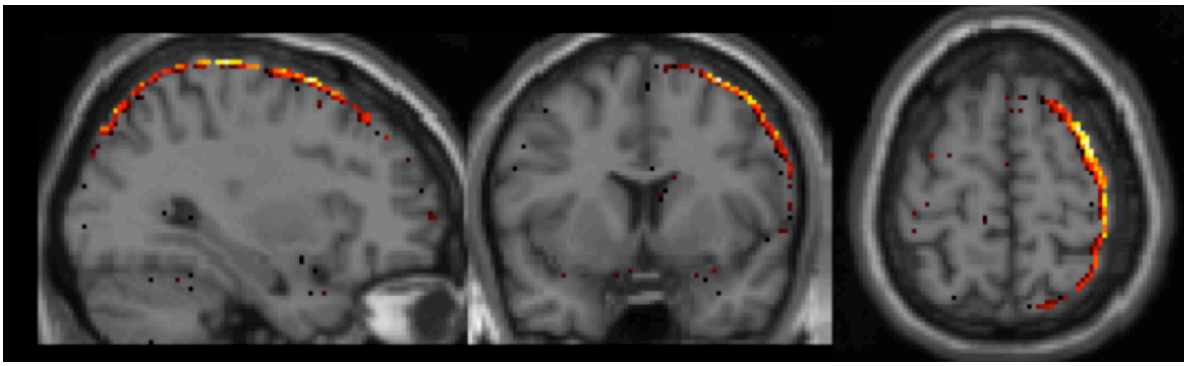

From the left is a sagittal (side), coronal (facing), and axial (overhead) view, respectively. Colored squares are areas of active voxels in this component. The yellow squares are where the greatest signal intensity levels were found.

The independent component estimation successfully extracted this movement-related noise into separate components distinct from viable networks. Further, it directed noise affecting voxels on the right side of subjects' brains into Component 1 as shown in Figure 8 and movement noise on the left side of the brain into Component 3, as shown in Figure 9.

Figure 9 Three orthographic views of Component 3

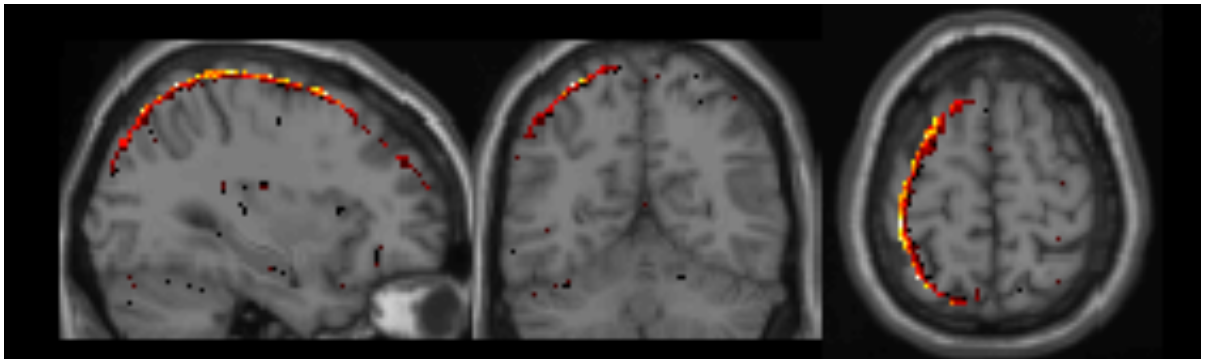

Images from left to right show views of the brain from the right side, from behind, and from above, respectively. The wide swath of active voxels across the left side of the brain is typical of patient movement-related noise.

The spectral graphs of components are essentially histograms of the Fourier transformations of the $\hat{\mathbf{a}}_j^+$, the component activations. They show the distribution of signal frequencies across time. Resting state signal frequencies are typically in the

range of 0.01-0.1 Hz (cycles per second), so signals outside of this range may be filtered out to improve the signal to noise ratio. A clear signal will transmit most of its signal within a narrow range of frequencies, concentrated at the mean. Component 6, presented in Figure 10 shows an example of this.

Figure 10 Spectral plot of Component 6

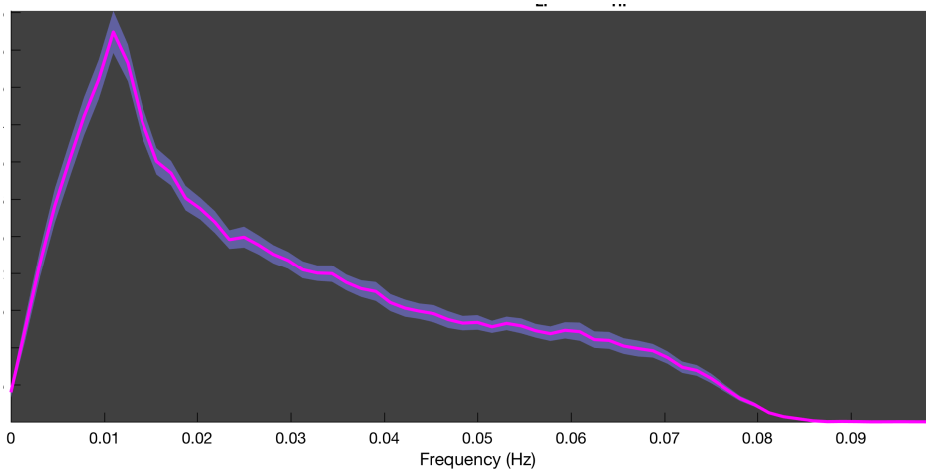

This figure, related to $\hat{\mathbf{a}}_6^+$, shows a reasonably clean signal with a mean frequency just over 0.01 Hz.

The spectral plot of Component 2, however, (shown in Figure 11), Component 4, and Component 5 are bi- or multi-modal, with more than one peak level of activation. This suggests that these three components may represent or be conflated by noise or signal interference.

Figure 11 Spectral plot of Component 2

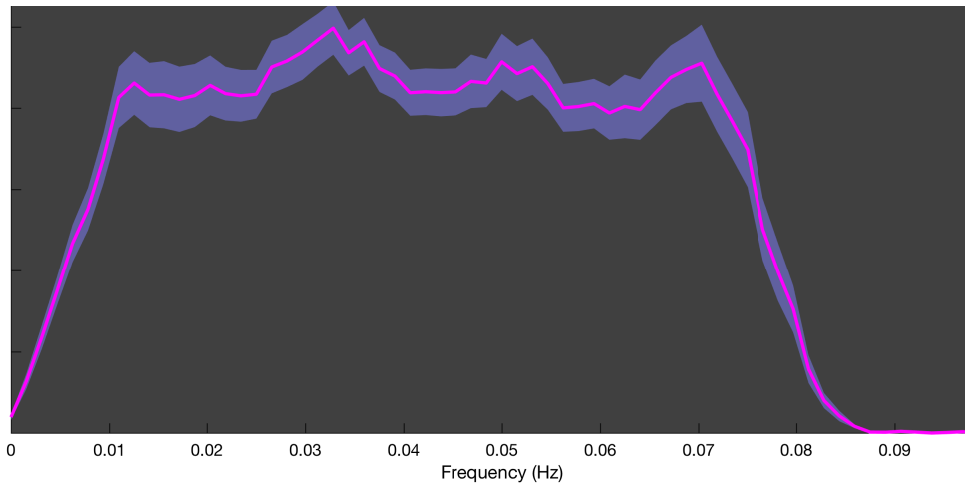

This shows a noisy signal. This may reflect noise or interference from other signals.

From the orthographic images of Component 2 (refer to Figure 12) and Component 5 (see Figure 13), i.e., $\hat{\mathbf{s}}_2$ and $\hat{\mathbf{s}}_5$, it does not appear that these components are noise-dominated, but neither do they reflect signals originating in neural structures (gray matter). The areas in which the active voxels appear are mostly within the ventricles of the brain, areas within the brain in which cerebral spinal fluid circulates and areas through which larger blood vessels of the brain pass. Cerebrospinal fluid (CSF) surrounds the brain and the spinal column providing both mechanical and biological protection to the neural structures. This fluid is not static, but pulsates as it is pumped through the spinal column and cranial cavity, similar to the movement of blood through the vascular system. In fact, if a subject's heart rate is 60 beats per minute, that represents a frequency of 0.0167, which is well within the range of expected signals from the fMRI scan.

Figure 12 Three orthographic views of Component 2

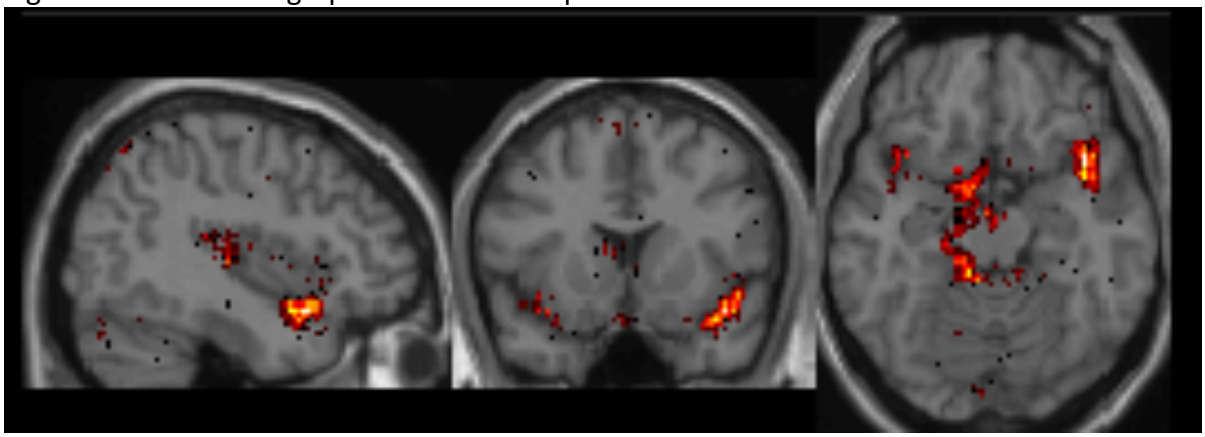

Views shown are sagittal (from the right side), coronal, (facing), and axial (overhead), respectively.

Figure 13 Three orthographic views of Component 5

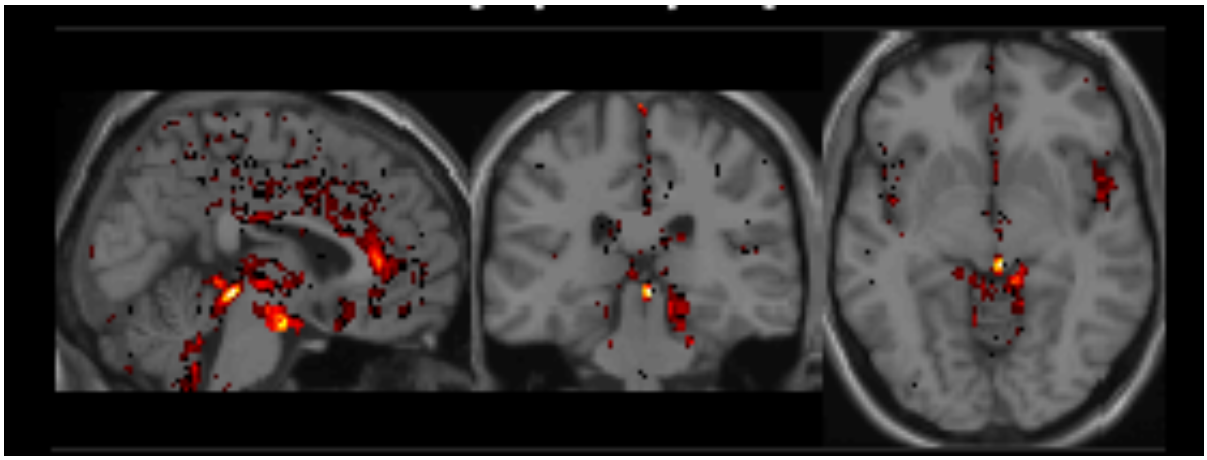

Views shown are sagittal (from the right side), coronal, (from behind), and axial (overhead), respectively.

Component 4 may not be obviously noise-dominated; however, the sagittal view of the orthographic images (the leftmost image) does suggest that this component could be dominated by movement-related noise because of the way the active voxels follow the curve where the skull and brain meet and is not from a more cohesive clump of voxels within the brain.

Figure 14 Component 4

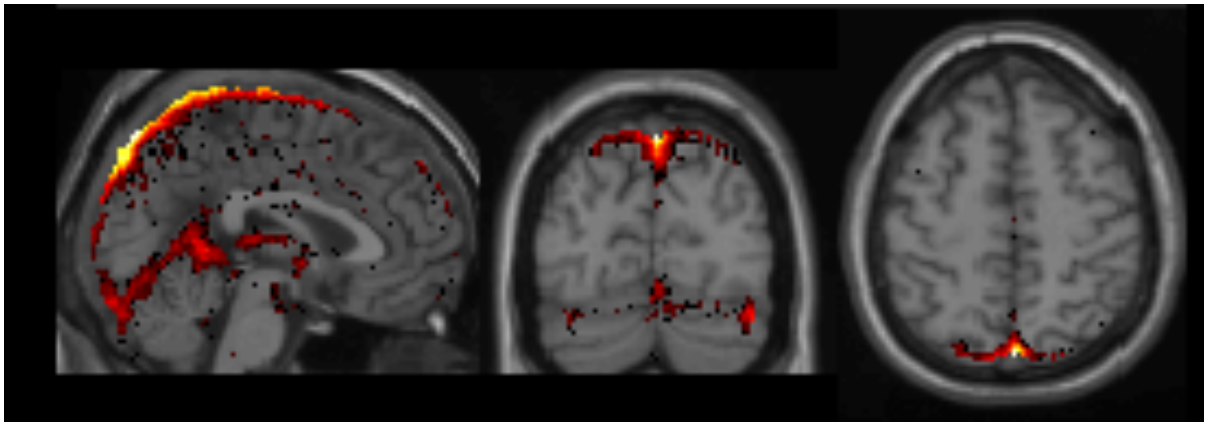

Figure shows a signal that is likely related to non-neural function. Views shown are sagittal (from the right side), coronal, (from behind), and axial (overhead), respectively.

The spectral plots, which reflect the activation time courses, $\hat{\mathbf{a}}_j^+$, provide an important clue to the sources of signals revealed in their paired spatial component, $\hat{\mathbf{s}}_j$. The information given by each are complementary and are frequently appropriate to consider in tandem.

Group-level Results—Basal Ganglia I

The basal ganglia region-of-interest test first considered the spatial correlation between the active voxels in each component, $\hat{\mathbf{s}}_j$, and the voxels that are located in areas within the basal ganglia template. The correlations of these components are indicated in Appendix D.

The degree of spatial correlation between the voxels of the components and voxels within the basal ganglia template was small: component 15, which was shown to have the highest correlation, had a correlation of just 0.038. Component 11 had a correlation of 0.014; the remaining components' correlations, including Component 13, were less than 0.01.

Figure 15 Component 15

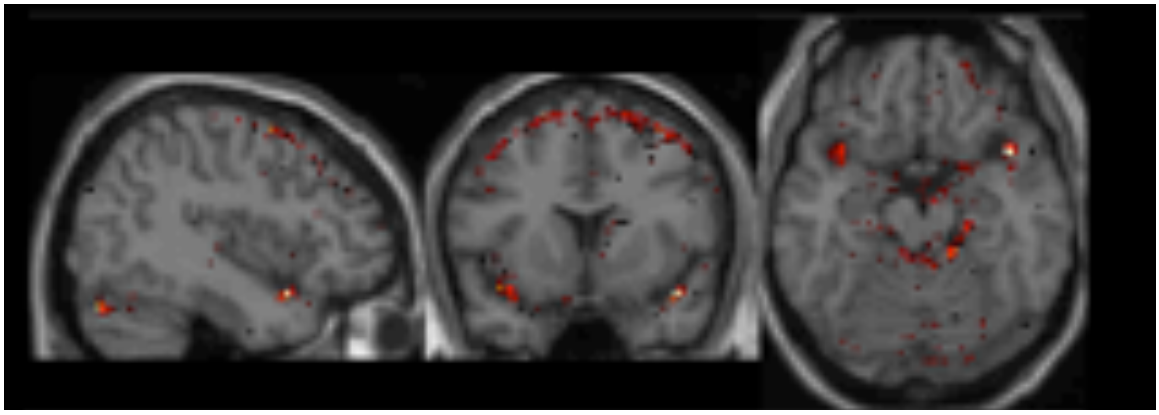

One of the components indicated as being correlated to the basal ganglia. Views shown are sagittal (from the right side), coronal, (facing), and axial (overhead), respectively.

Group-level Results—Basal Ganglia II

In addition to identifying components using a specific ROI, each component was matched with one of the brain networks, based on the correlation between its spatial maps and the brain regions defined by a standard atlas. Refer to Figure 7 for an example of a basal ganglia atlas and to Appendix A for examples of other known brain network maps. The regions assigned to each of the 20 components are presented in Appendix G. By this analysis, only one component, number 13, was considered likely to be related to the basal ganglia; however, the correlation in this assessment was only 0.091.

Figure 16 Component 13

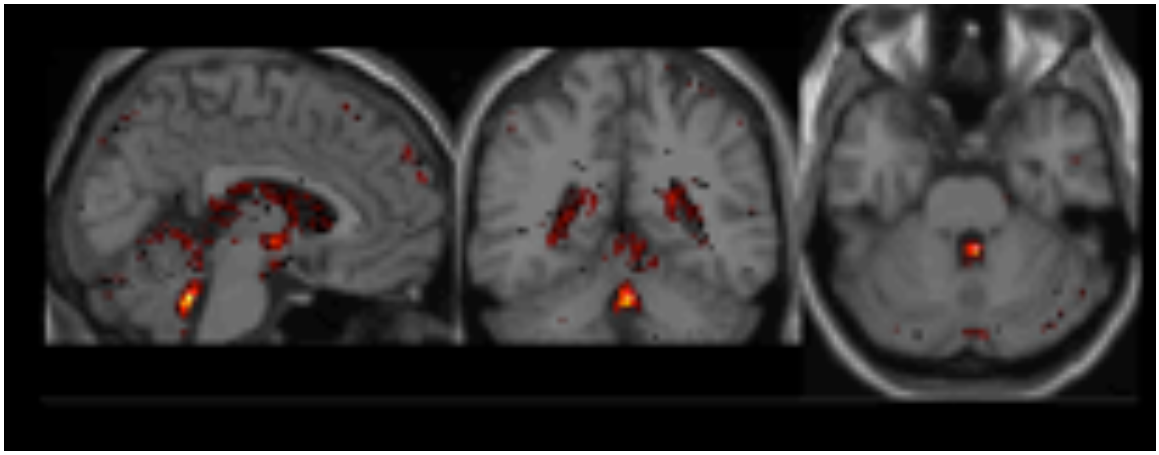

The component which was labeled as most correlated to the basal ganglia in the component labeling function of GIFT. Views shown are sagittal (from the right side), coronal, (from behind), and axial (overhead), respectively.

The amount of correlation reported between the components and the networks they were mapped to was low, which suggests either that the amount of overlap between the components and their respective templates was modest or the sample size was inadequate. Among the components, only four had correlations with their respective templates above 0.20: Components 9, 1, 11, and 8. Refer to Appendix G for details.

There were four networks in the atlas templates used by the software application that were not assigned to any of the components: those related to vision, visuospatial processing, language, and hearing all of which are functional areas that would not be expected to be active during a resting-state study.

Subject-level Results

Histograms of the subject-level components' activation levels, $\hat{\mathbf{s}}_{ij}$, revealed small or slight differences in peak values in about half of the components. In all of these, the histograms of the Parkinson's disease study group had higher mean peaks than the control subjects.

Differences between the groups' activations were small enough that they could be due to chance; however, in all cases the taller histogram was that of the study group. This would suggest a small, but systematic difference between the study groups.

As shown in Table 1, there were significant differences between the groups in both age and sex. There is a known association between age and changes in cognitive function; the differences between the study groups' histograms may be a reflection of this. The histograms are shown in Appendix F.

Primary Endpoint

Differences in voxel activity levels between the two study groups were assessed using a voxel-wise generalized linear regression with voxel activation level as the outcome and the number of months since diagnosis (as a proxy for severity) as the predictor, adjusting for age and sex.

The regression models were fitted using the following equation:

$$\hat{\mathbf{s}}_j(k)=\text{Months since diagnosis}+\text{Sex}+\text{Age}+\epsilon,$$

for component j, where k=1, 2 ,..., 190,446 and $\hat{s}_j(k)$ is the kth active voxel in component j.

After each regression model was fitted for each voxel, we recorded the p-values of the coefficients on the "months since diagnosis" variable to create a "p value map" of a model brain for each component. This would give a brain map of voxels that were significantly affected by the presence of the disease and its longevity. (Each component image would be like those seen in the above figures, but instead of a map of activation levels, it would show a map of statistically significant regression model coefficients.)

However, the regression models did not show a significant effect of disease status on the voxel activation levels. After correcting for multiple comparisons, the FDR[3]-

[3] False discovery rate, for details see Benjamini & Hochberg (1995)

corrected p values were not significant. Refer to Appendix C for regression model output. In addition, the fit of the regression models was poor. Model output from random samples of voxels showed that model fit was non-significant and adjusted R-squared values were exceedingly low, frequently negative.

There did not appear to be any systematic differences in the activation levels between the study groups for any of the components, after adjusting for sex and age and correcting for multiple comparisons. Summary statistics of the adjusted p values on the regression coefficients are presented in Appendix C.

Discussion

Analysis Results

The primary aim of this study was to determine if component sources estimated with ICA would demonstrate differences in functional MRI activation levels and, if so, could they be used to differentiate subjects with Parkinson's disease from control subjects. We performed linear regressions using voxel activation level as the dependent variable and disease status as the predictor of interest, adjusting for sex and age.

The regression equations were fitted across all components, using each active voxel as the dependent variable. The unadjusted significance level of the coefficient on each voxel was retained after its regression was run. The number of regressions in which the coefficient was nominally significant (≤0.05) was no greater than would be expected by chance. In none of the 20 estimated components did the proportion of significant p-values on the voxels' regression coefficients approach 0.10. After adjusting for multiple comparisons, only two components were left with any statistically significant regression coefficients.

The results of the ROI analyses were contradictory. In the first ROI analysis, component 15 was reported as the component that was most highly correlated with the basal ganglia, although its correlation was only 0.038. Other than component 11, the remaining components' correlations with the basal ganglia were less than 0.01.

Component 13 was the least correlated to the basal ganglia, with a reported correlation of 0.000173 (result not presented).

In the second analysis, in which all components were labeled with the network they were most correlated with, component 13 was the only component given the label of "basal ganglia," even though the reported correlation was low, at 0.091, there was no other network that this component was more closely correlated with.

While not definitive, manually matching the components using the network maps presented in Appendix A, showed component 13 as most closely overlapping with the basal ganglia map, compared to the other networks shown.

Study Limitations

Identification of the basal ganglia, as the target region of interest was inconsistent within the GIFT application, as there was no single component which appeared to be clearly related to the structures within the basal ganglia. This was disappointing and we were unable to draw any conclusion on the effects of Parkinson's disease on the functional images of the subjects within our study.

Estimating subject-level data from group-level independent components is currently regarded as an appropriate method for performing study group comparisons with independent components. However, it is unknown to what extent subject-level variability is preserved (or restored) within subject-level components versus the extent to which it is dampened by the strength of the group-averaged components used to estimate them. It seems possible that individual differences are more relevant than averaged group-level differences. However, it is not possible to compare components estimated using independent component analysis on the data from single subjects because of the stochastic nature of the estimation procedure.

We discovered that ROI analyses within GIFT needed to be performed with some degree of caution. In this study, different approaches reached very different conclusions, even though spatial correlation was used as the metric.

Conclusion

Functional MRI data can provide insight into human cognitive processes and is potentially a very rich source of data. Although independent component analysis is useful as a method for making such complex data more manageable, in analyses that compare subject-level or group-level differences, independent component analysis can only be used as the first step, although it can provide valuable information as a starting point for further, more in-depth analyses.

Appendices

Appendix A Mapped Resting-State Brain Regions

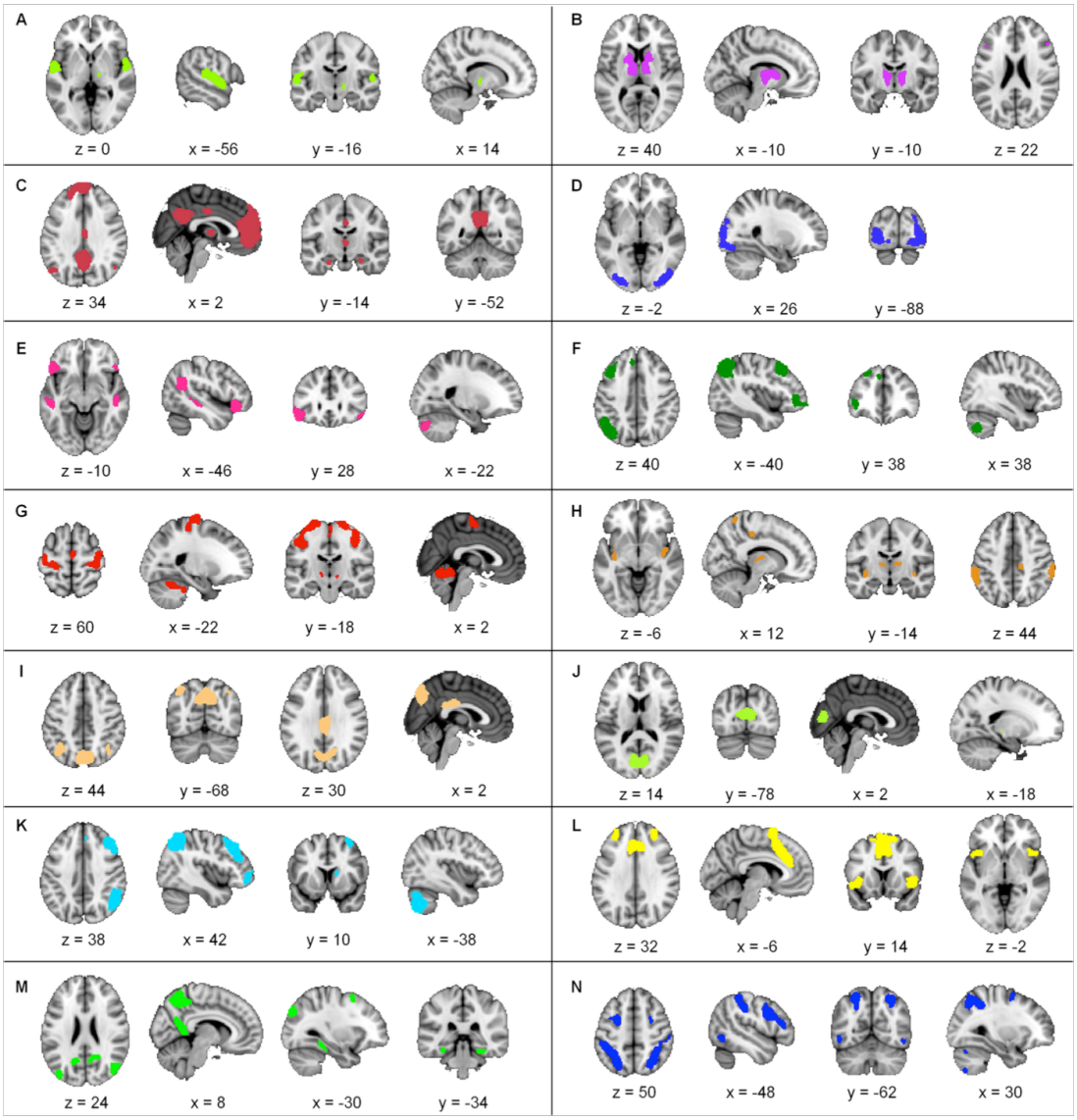

Figure S2. Fourteen intrinsic connectivity networks identified in resting-state data by group ICA. This figure shows the ROIs contained within each ICN. (*A*) Auditory, (*B*) Basal Ganglia, (*C*) Posterior Cingulate Cortex (PCC)/Medial Prefrontal Cortex (MPFC), (*D*) Secondary Visual Cortex (V2), (*E*) Language, (*F*) Left Dorsolateral Prefrontal Cortex (DLPFC)/Left Parietal Lobe, (*G*) Sensorimotor, (*H*) Posterior Insula, (*I*) Precuneus, (*J*) Primary Visual Cortex (V1), (*K*) Right Dorsolateral Prefrontal Cortex (DLPFC)/Right Parietal Lobe, (*L*) Insula/Dorsal Anterior Cingulate Cortex (dACC), (*M*) Retrosplenial Cortex (RSC)/Medial Temporal Lobe (MTL), (*N*) Intraparietal Sulcus (IPS)/Frontal Eye Field (FEF).

Figure appears as supplemental material in: Shirer, W. R, S Ryali, E Rykhlevskaia, V Menon, and M. D Greicius. 2012. "Decoding Subject-Driven Cognitive States with Whole-Brain Connectivity Patterns," Cerebral Cortex 22, 22 (1): 158–65; used by permission of Oxford University Press. Shown with original caption from source.

Component Images—Key

Component Number (j)

Activation Time Course, $\hat{\mathbf{a}}_j^+$

Shows the activation of each group-level component as the average across all subjects: $\hat{\mathbf{a}}_j^+ = \frac{\sum_{i=1}^{M} \hat{a}_{ij}^+}{M}$. Can give an indication of movement noise as seen in an abrupt change in the waveform, e.g.

Power spectral density plot:

Shows a measure of power by frequency of the time-sampled signals. Gives an indication of how "clean" the signal is by showing the range and proportion of frequencies in each component. An ideal signal would show a narrow spike of energy at its mean frequency.

Rendered Image

Spatial map, $\hat{\mathbf{s}}_j$ as it would appear in a 3-D model of a brain. Six different views are shown, arranged as indicated below:

From below	From above
Right side	Left side
Facing	From behind

Orthographic Image

Internal view of component's spatial map, $\hat{\mathbf{s}}_j$, at a selected location with peak activation. Spatial (x, y, z) coordinates of the central voxel are given. Views are, from left to right: sagittal (side view), coronal (facing), and axial (overhead). Color bar shows range of t scores

Appendix B Images of the 20 Estimated Components

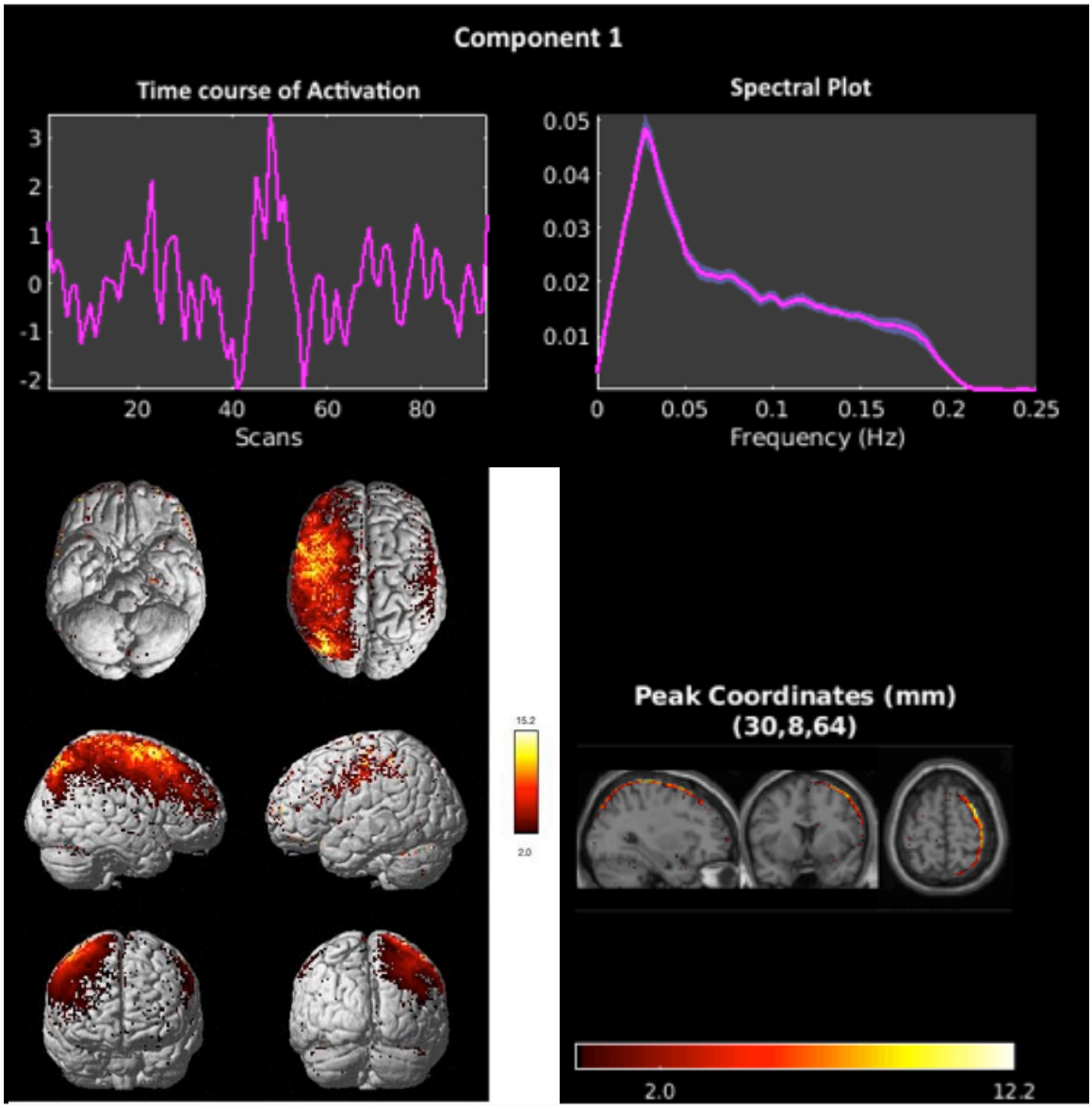

Appendix B Images of the 20 Estimated Components

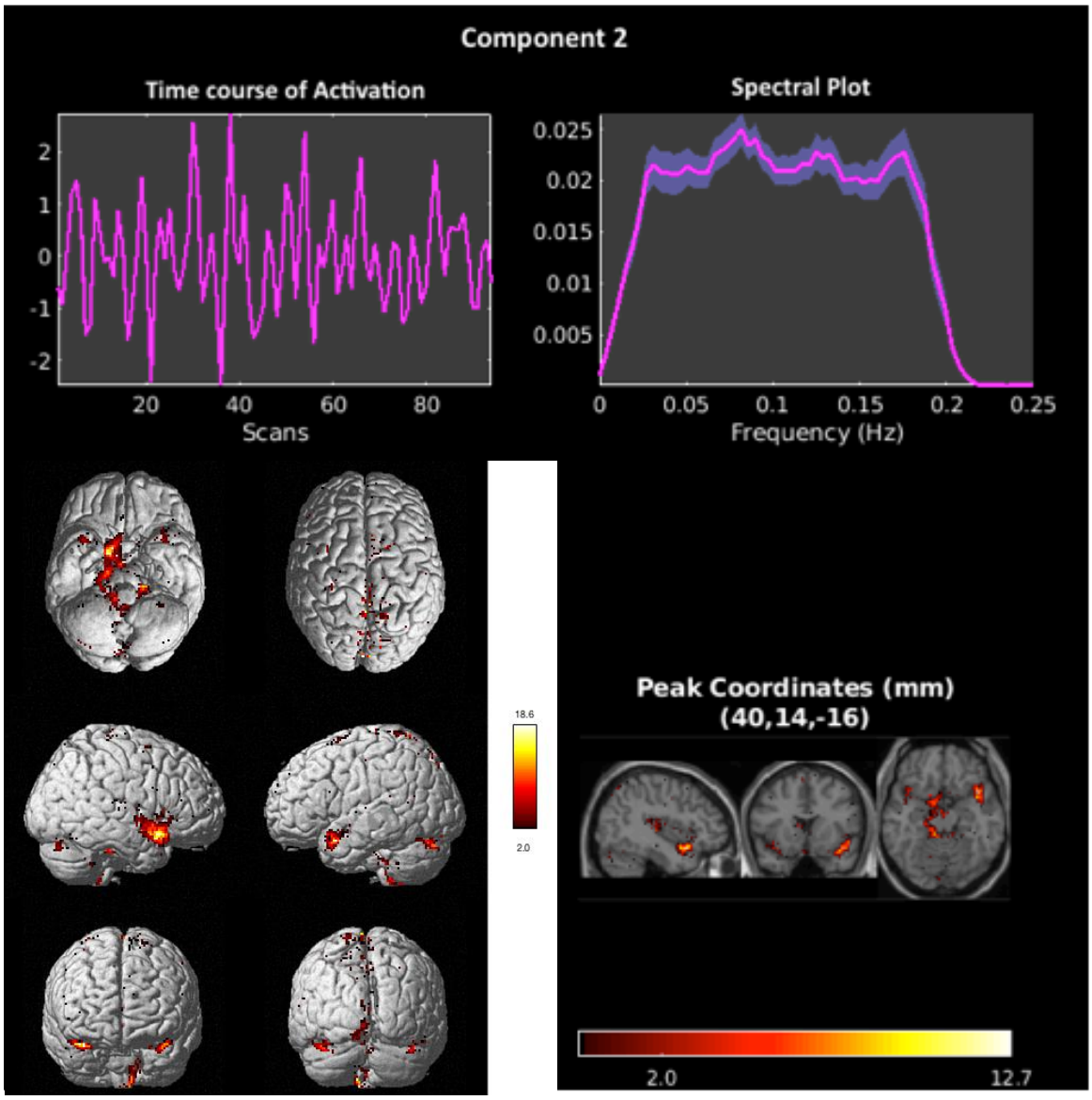

Appendix B Images of the 20 Estimated Components

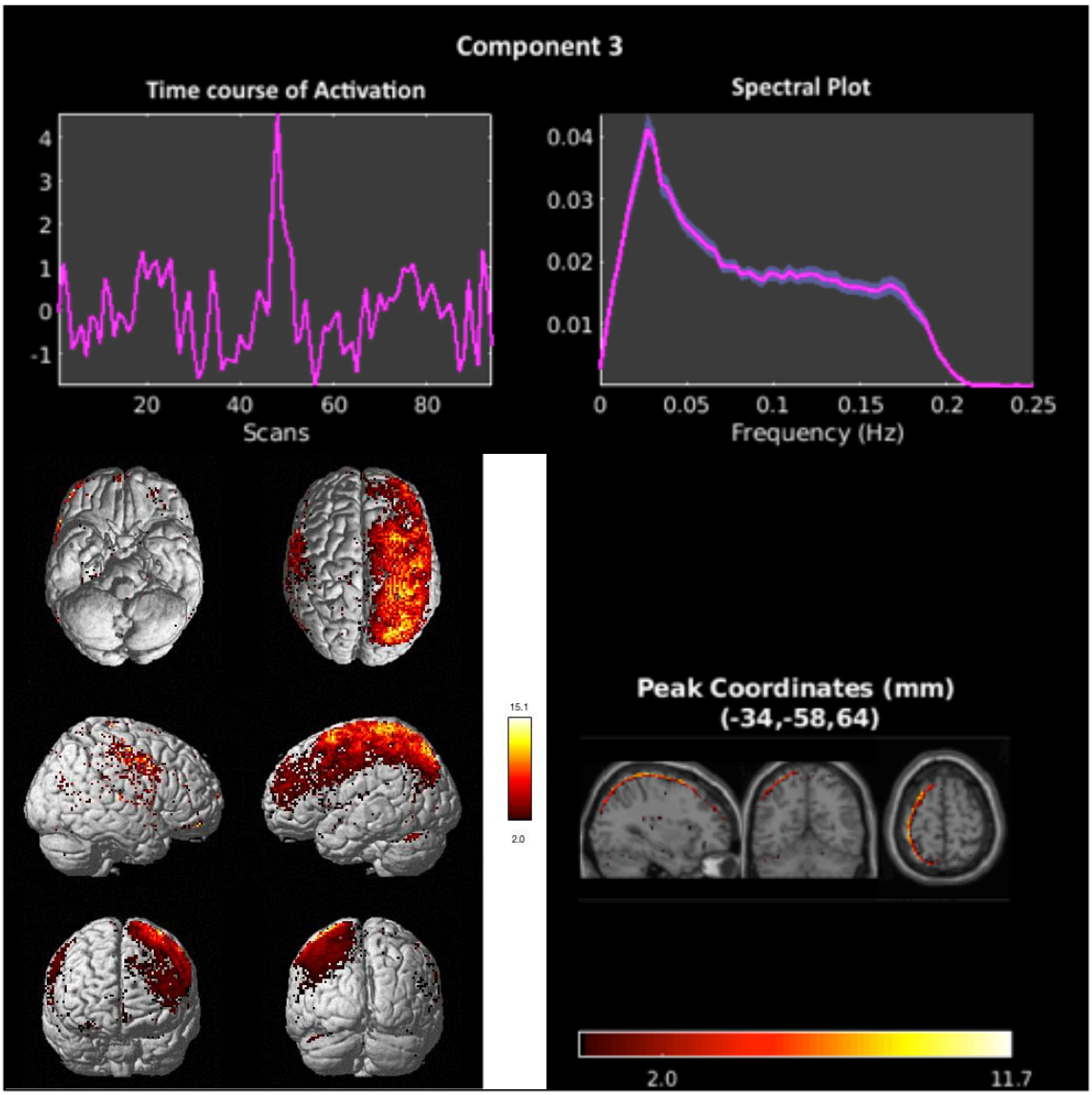

Appendix B Images of the 20 Estimated Components

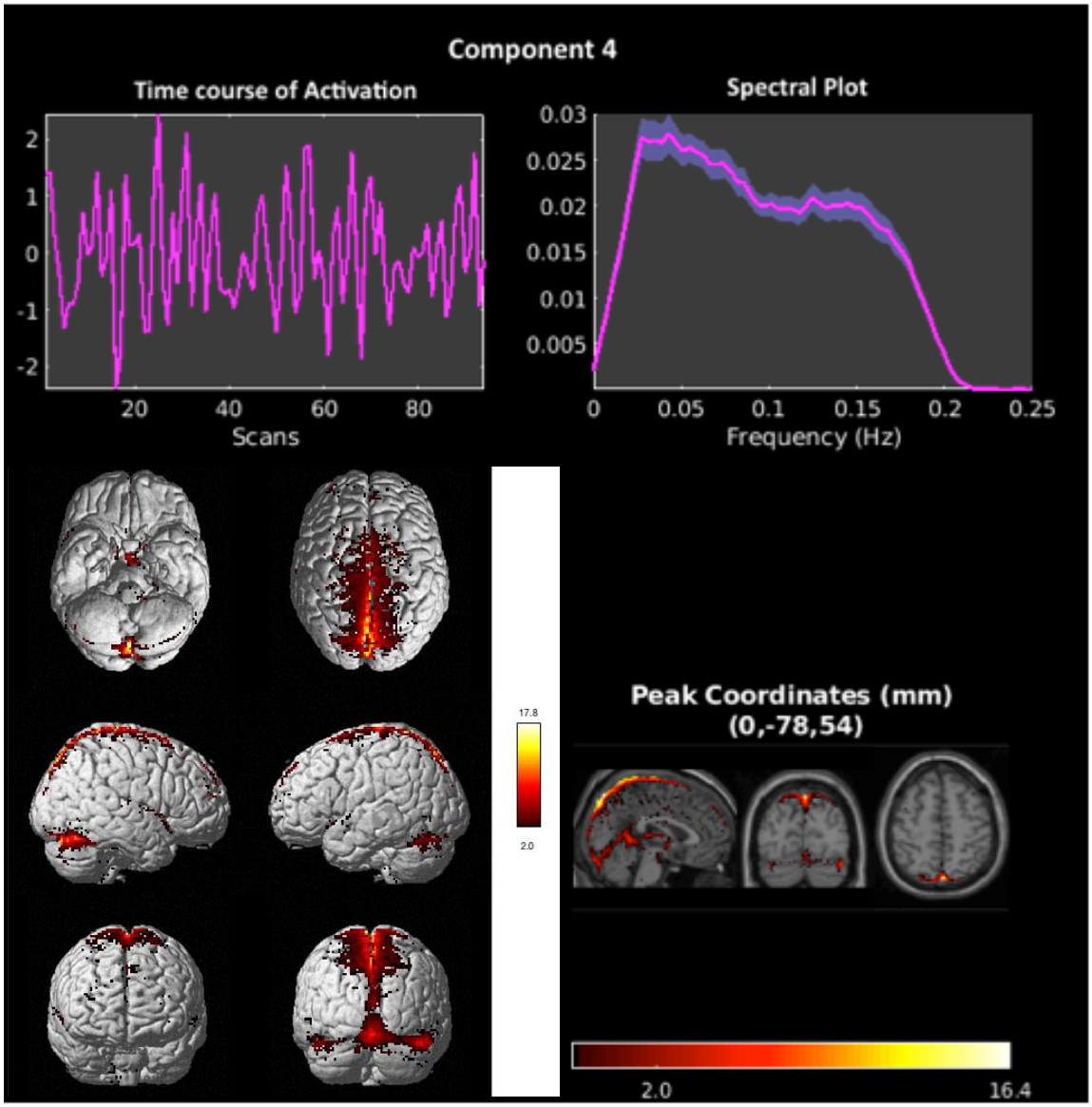

Appendix B Images of the 20 Estimated Components

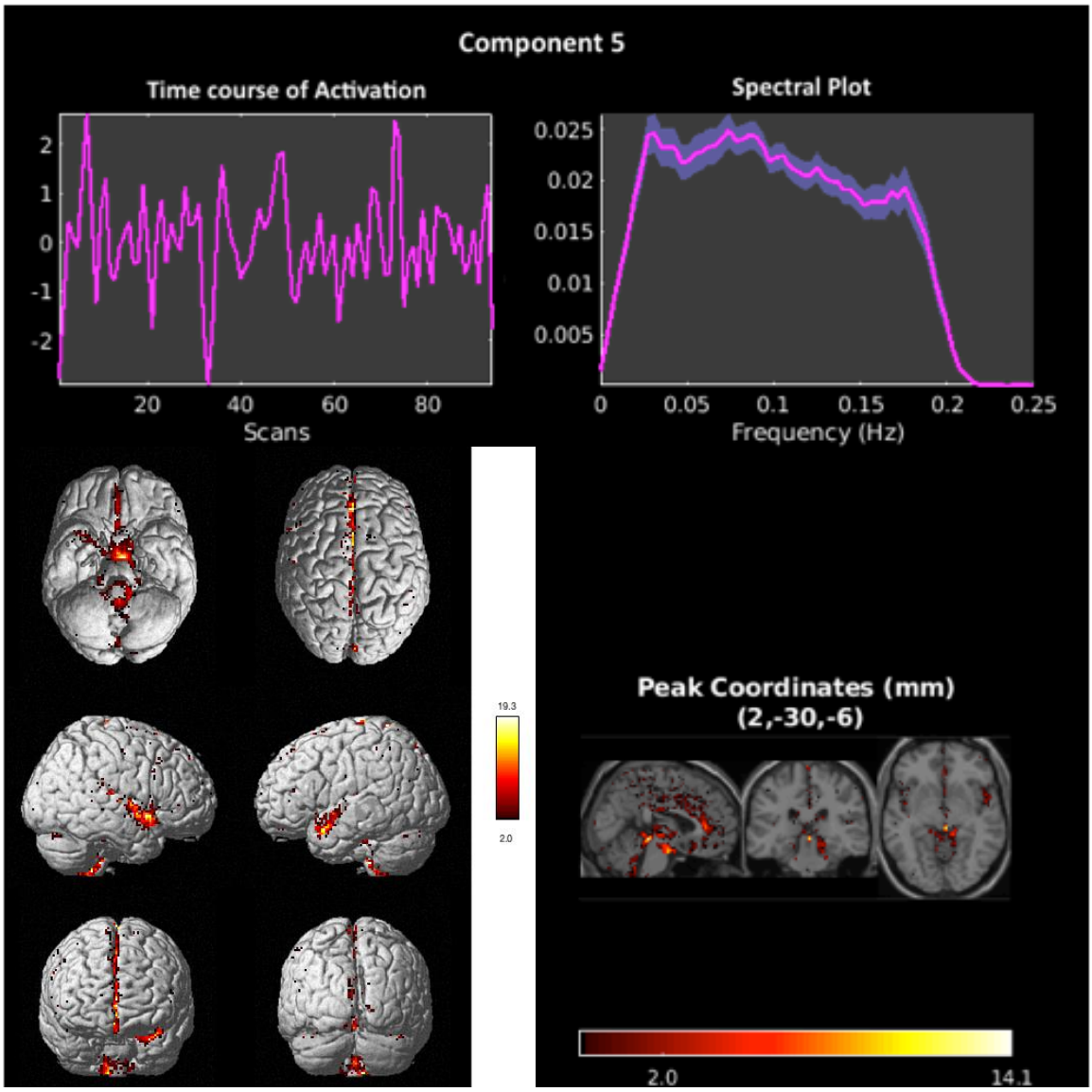

Appendix B Images of the 20 Estimated Components

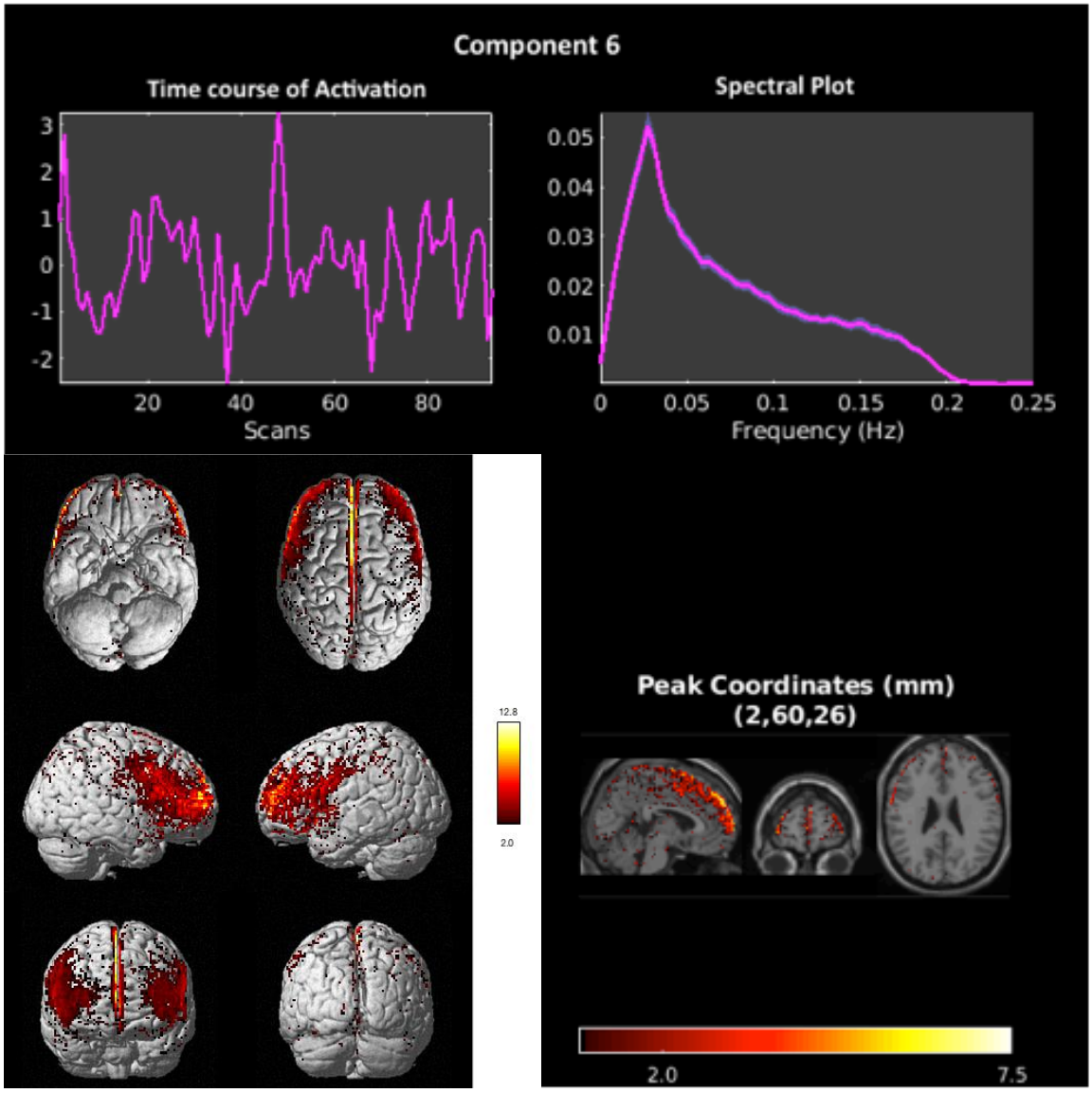

Appendix B Images of the 20 Estimated Components

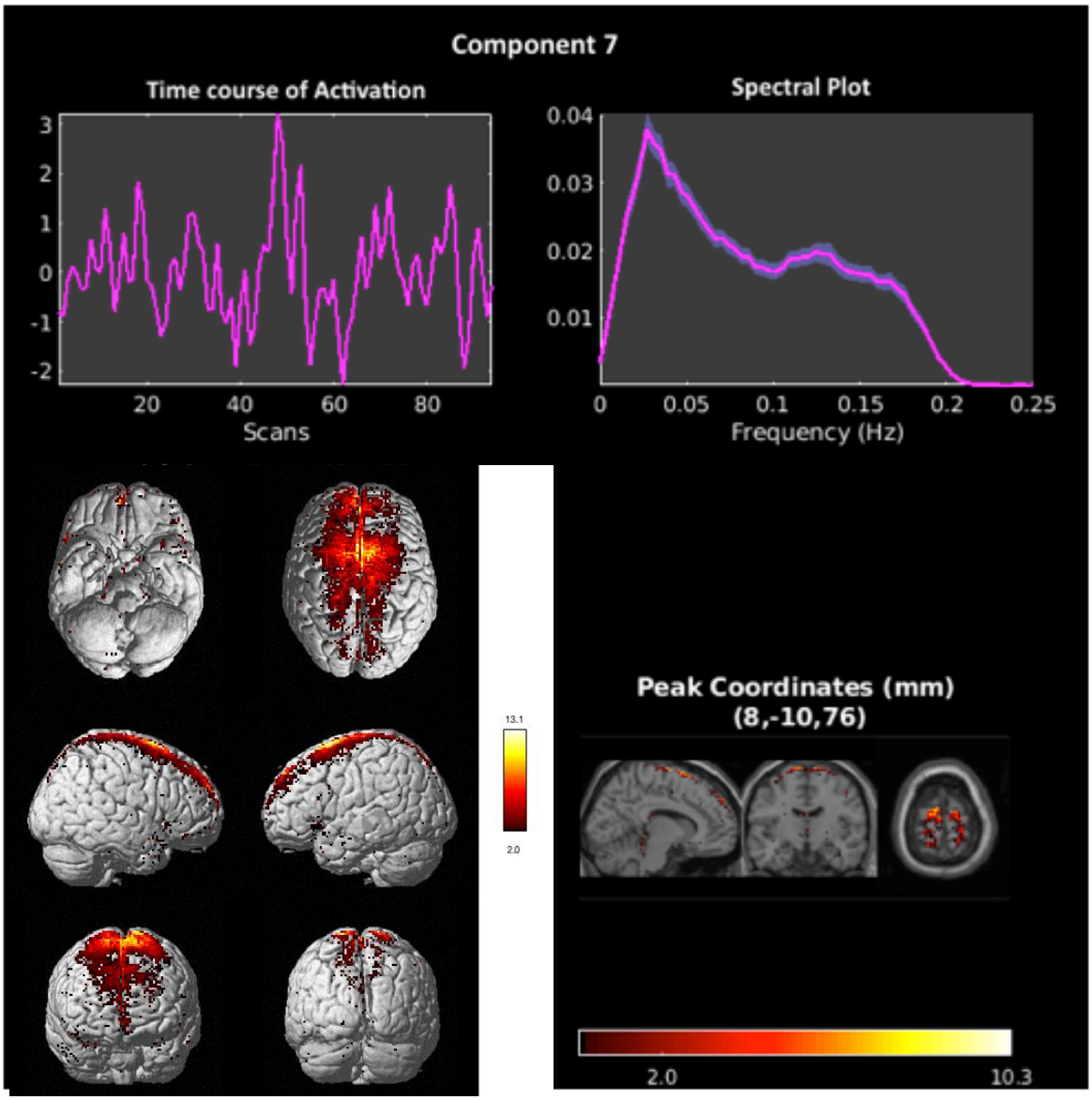

Appendix B Images of the 20 Estimated Components

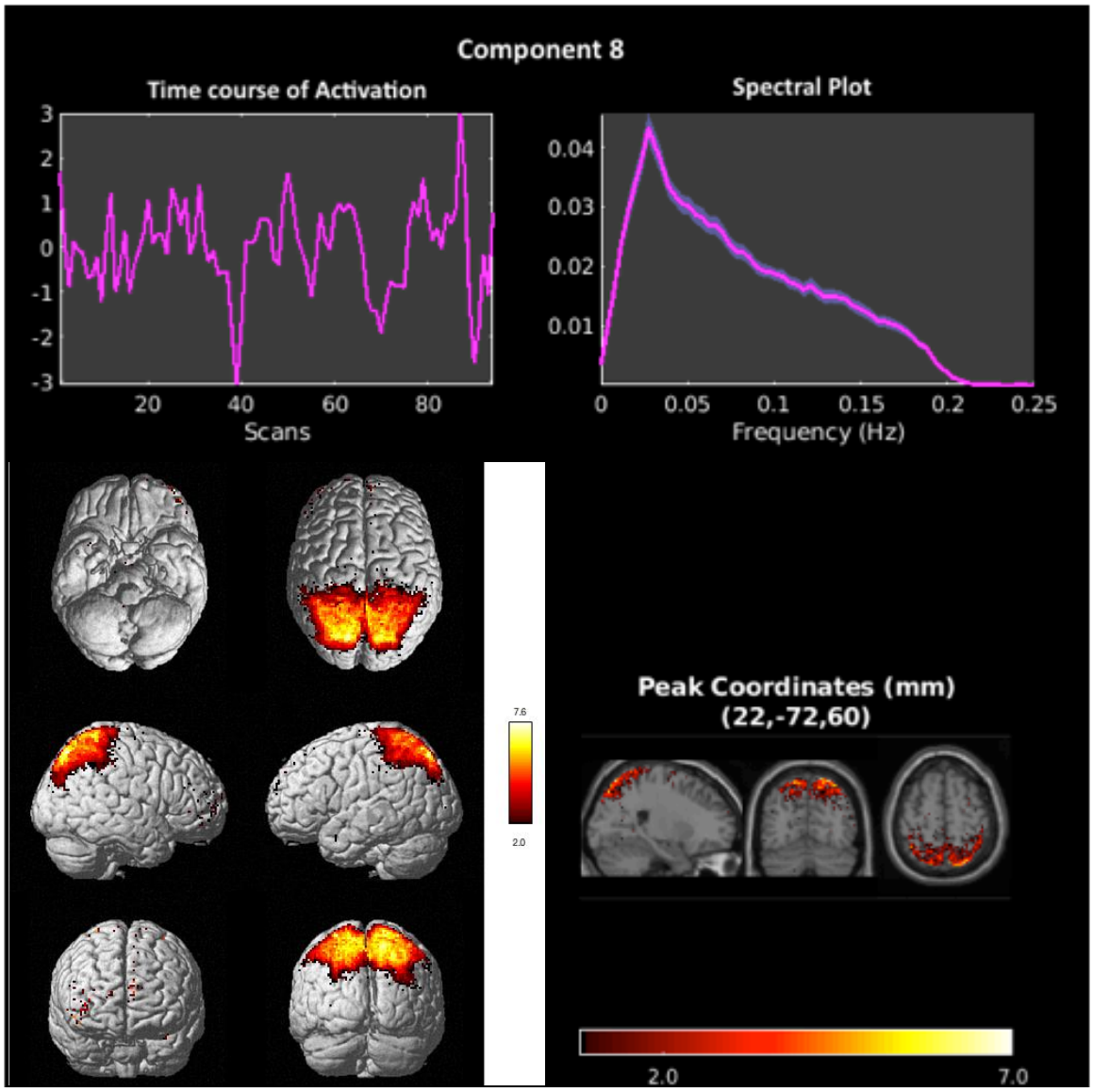

Appendix B Images of the 20 Estimated Components

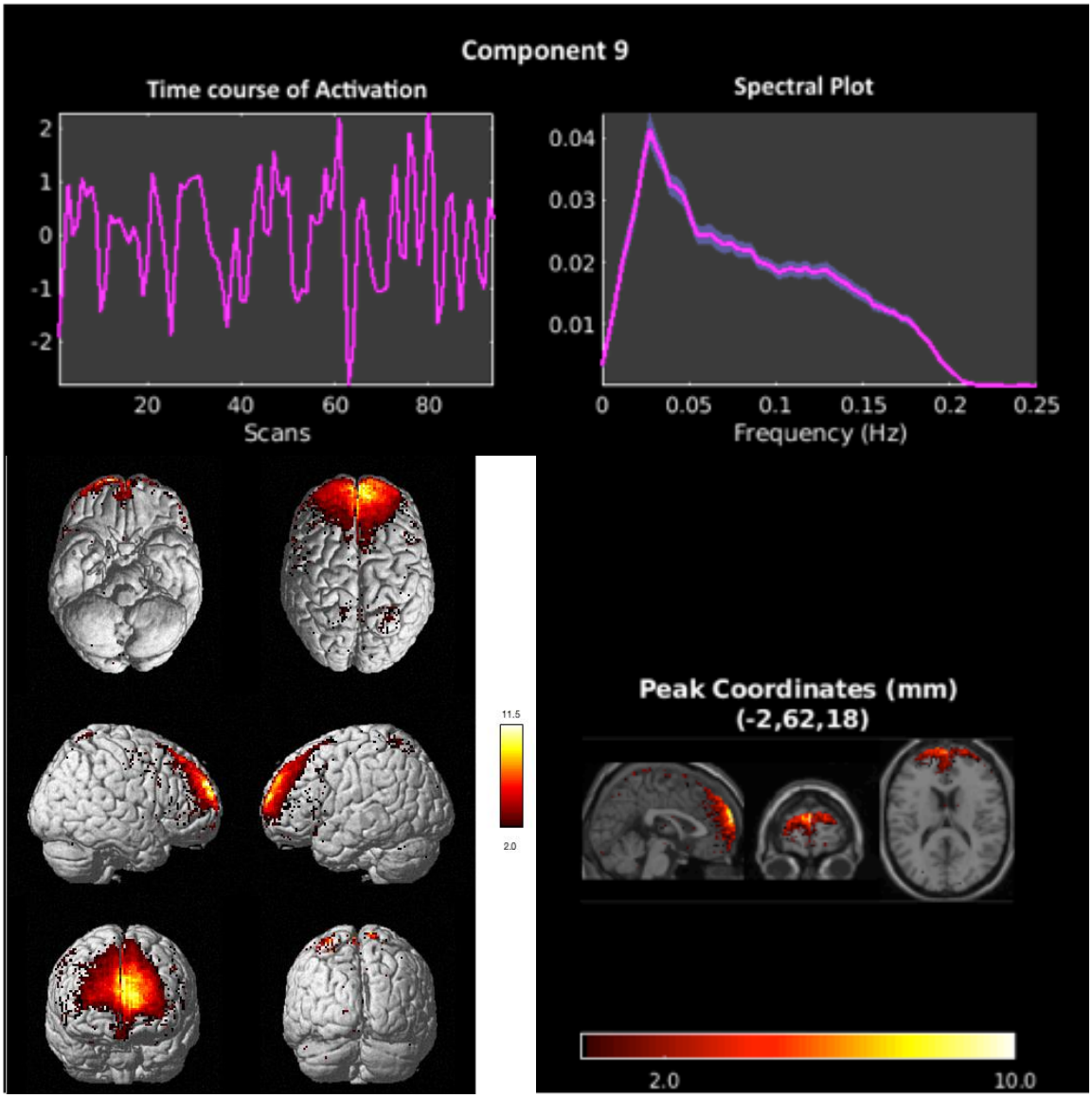

Appendix B Images of the 20 Estimated Components

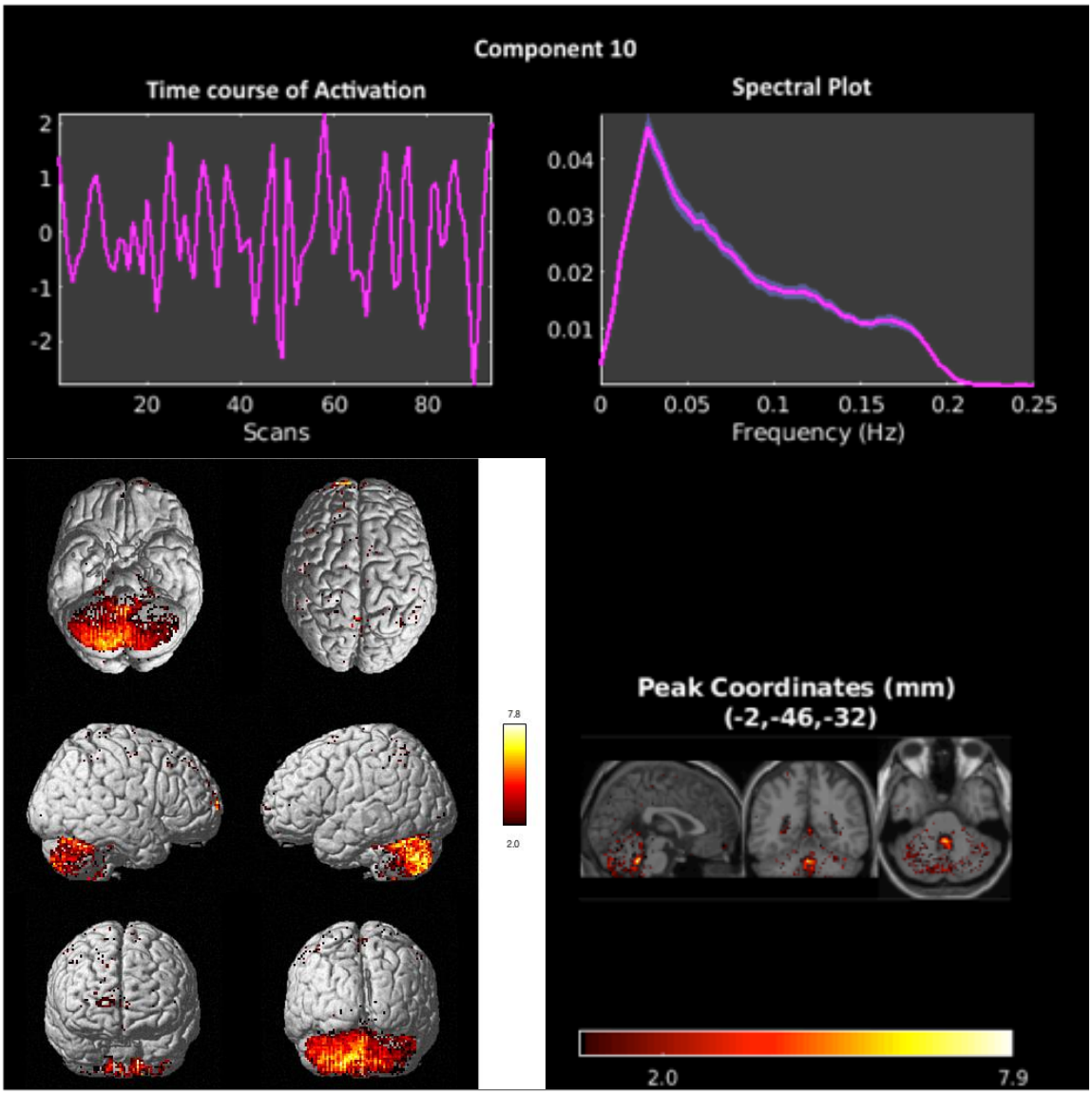

Appendix B Images of the 20 Estimated Components

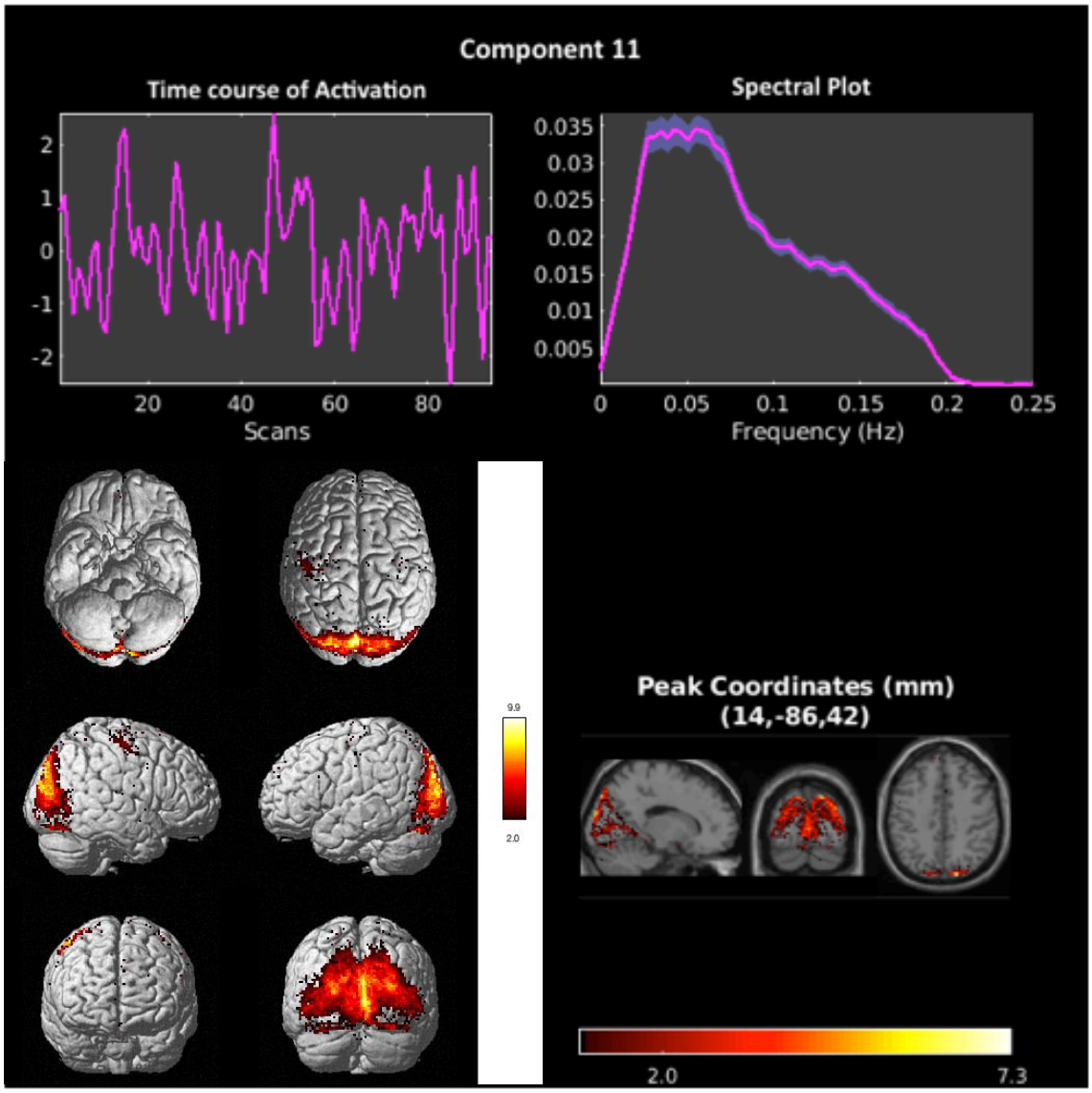

Appendix B Images of the 20 Estimated Components

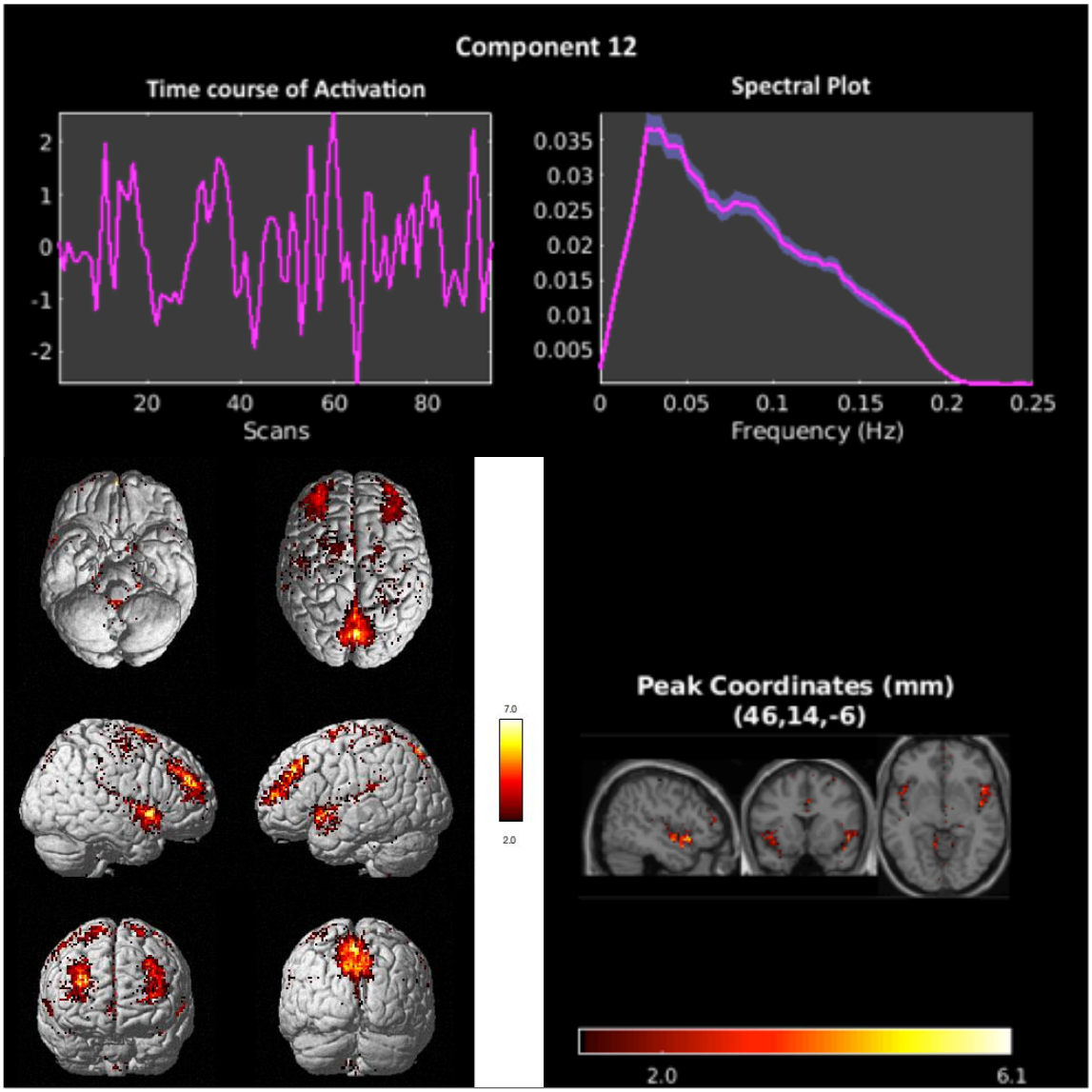

Appendix B Images of the 20 Estimated Components

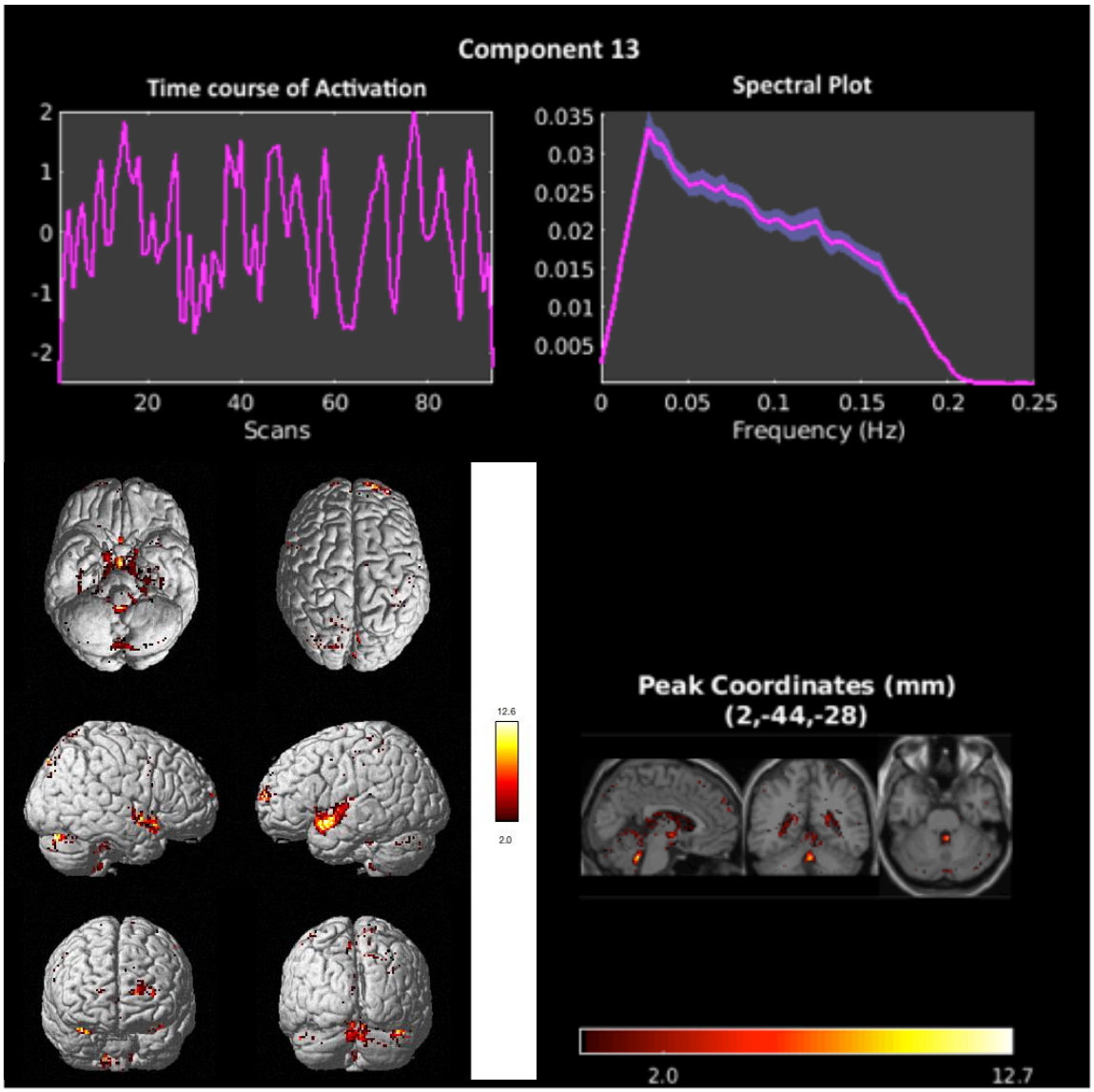

Appendix B Images of the 20 Estimated Components

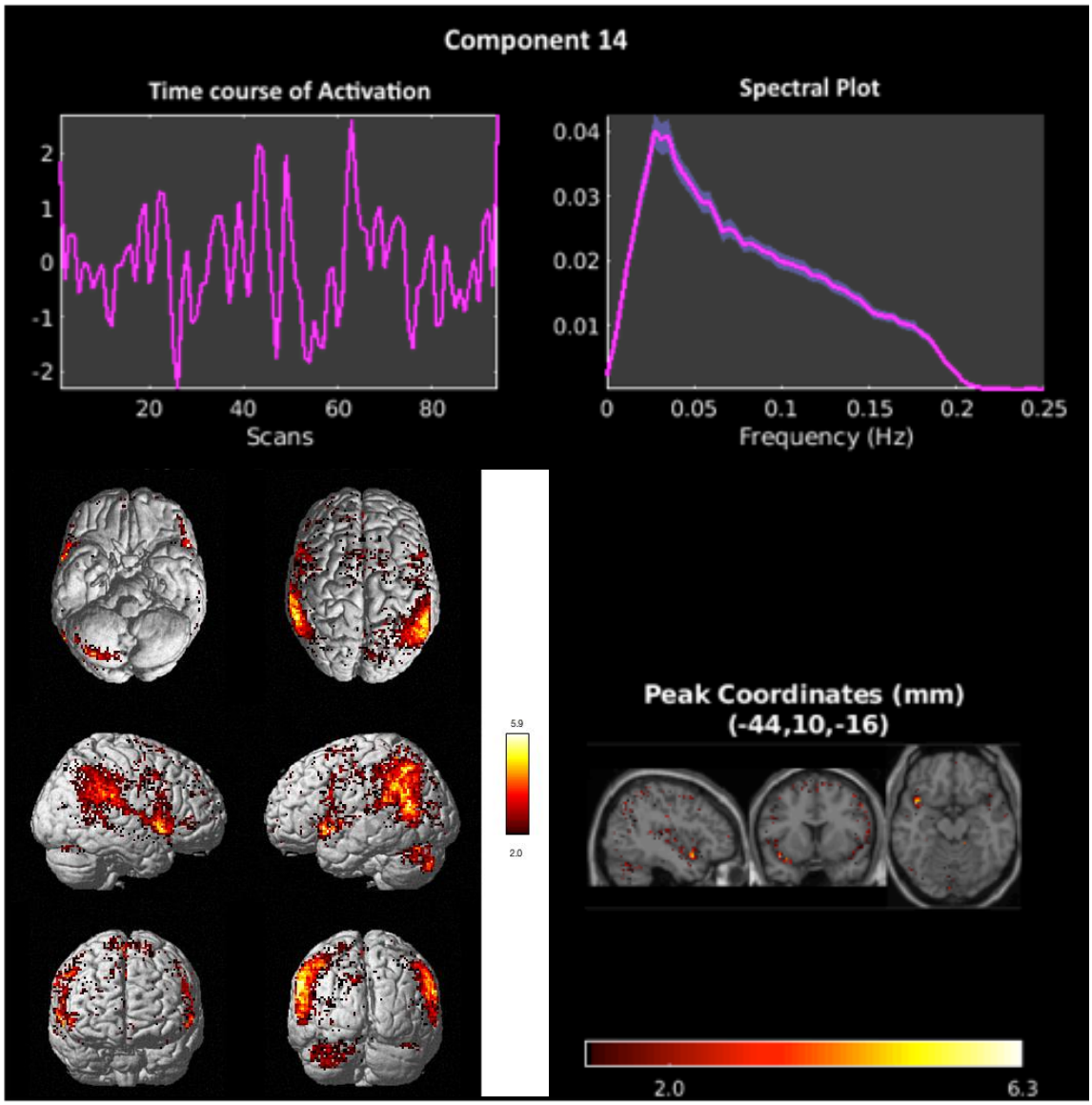

Appendix B Images of the 20 Estimated Components

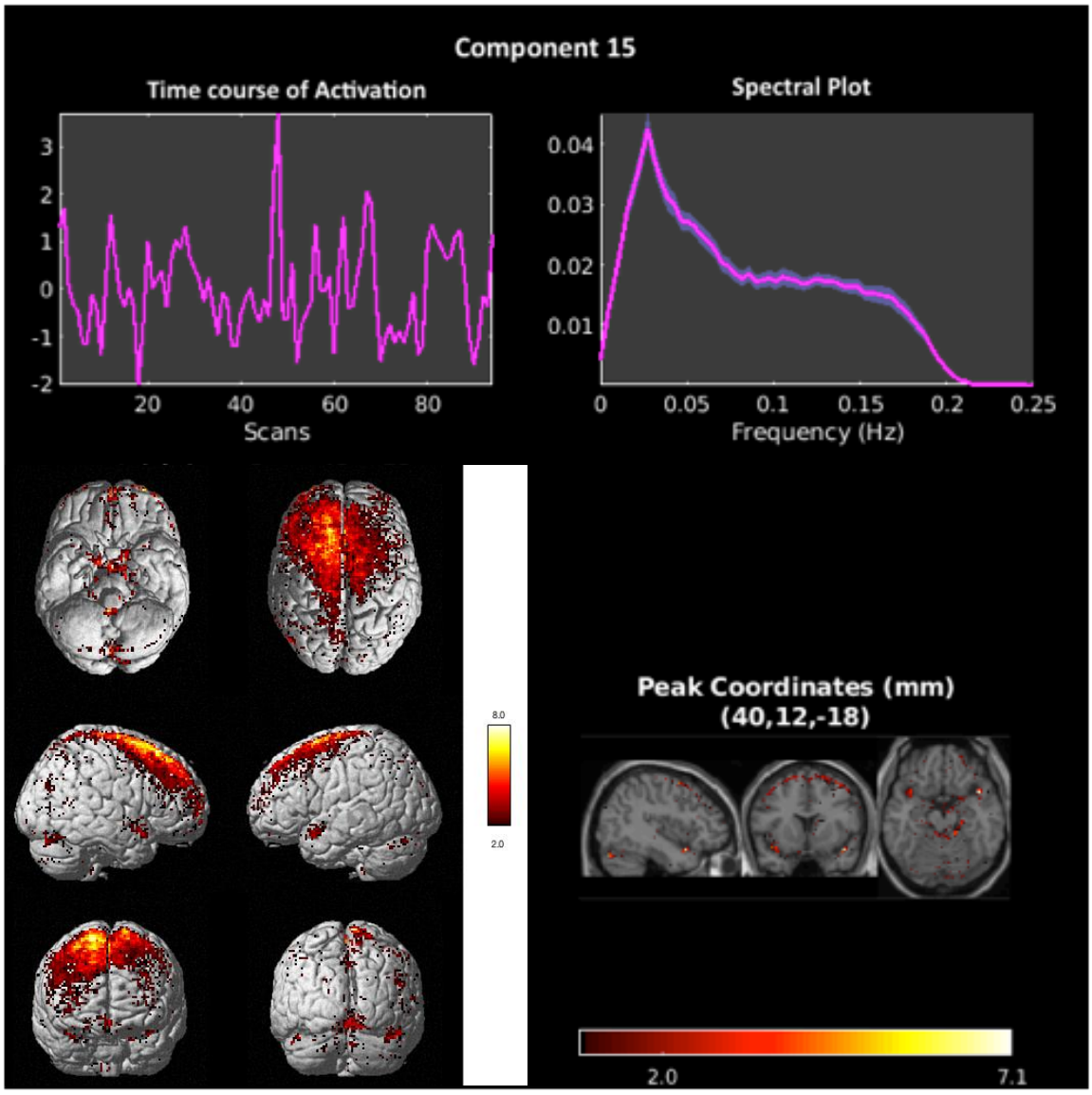

Appendix B Images of the 20 Estimated Components

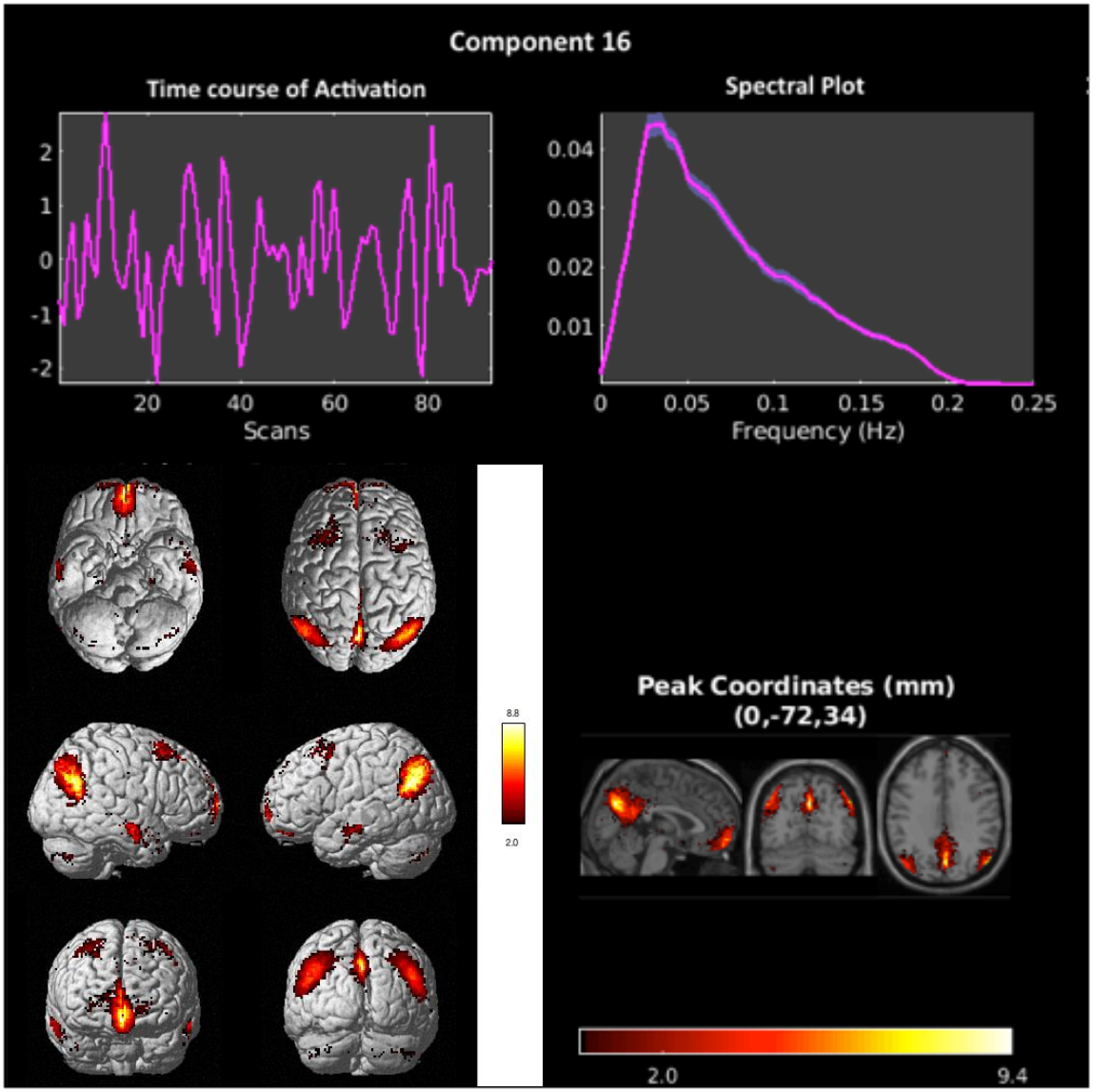

Appendix B Images of the 20 Estimated Components

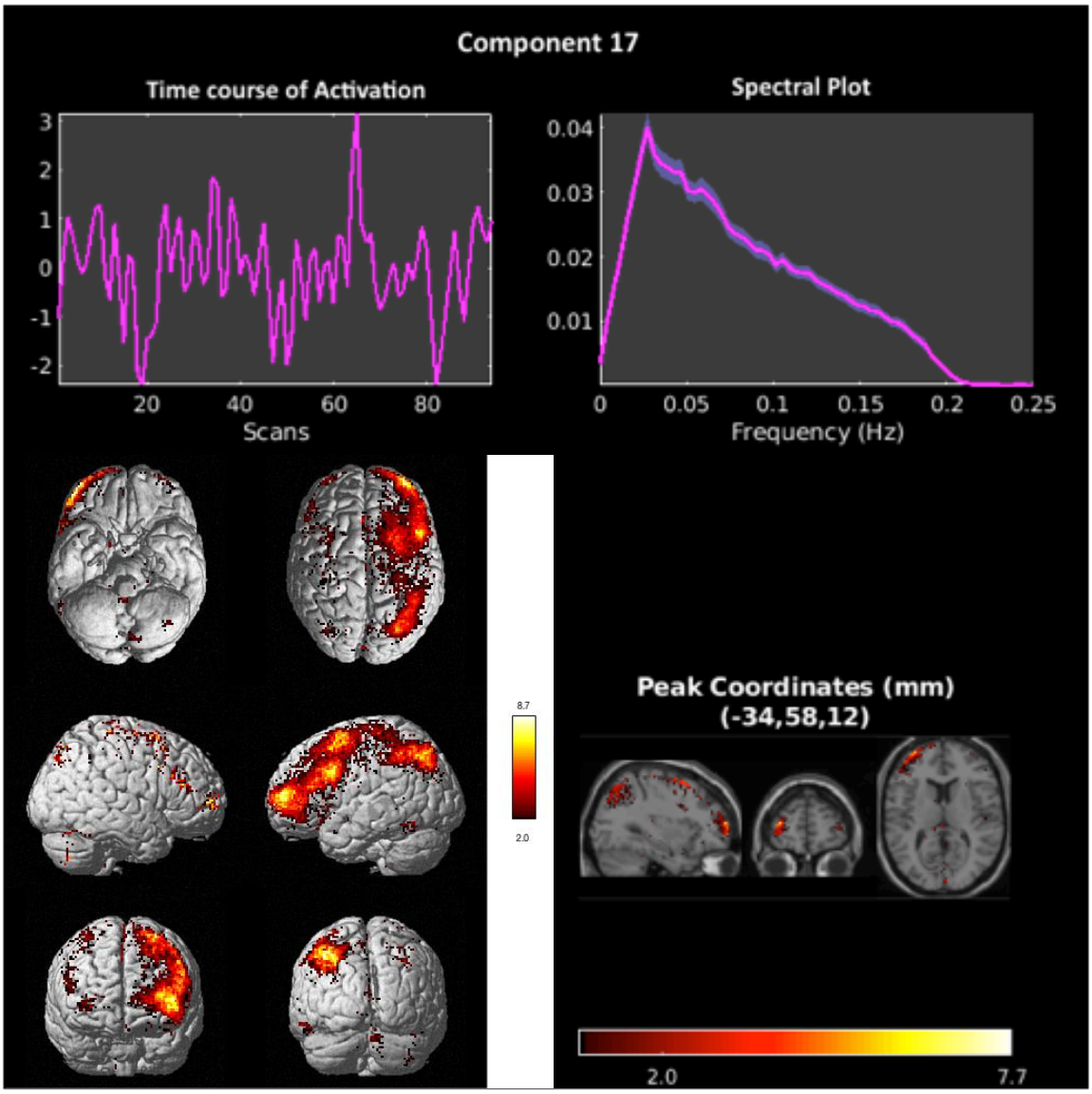

Appendix B Images of the 20 Estimated Components

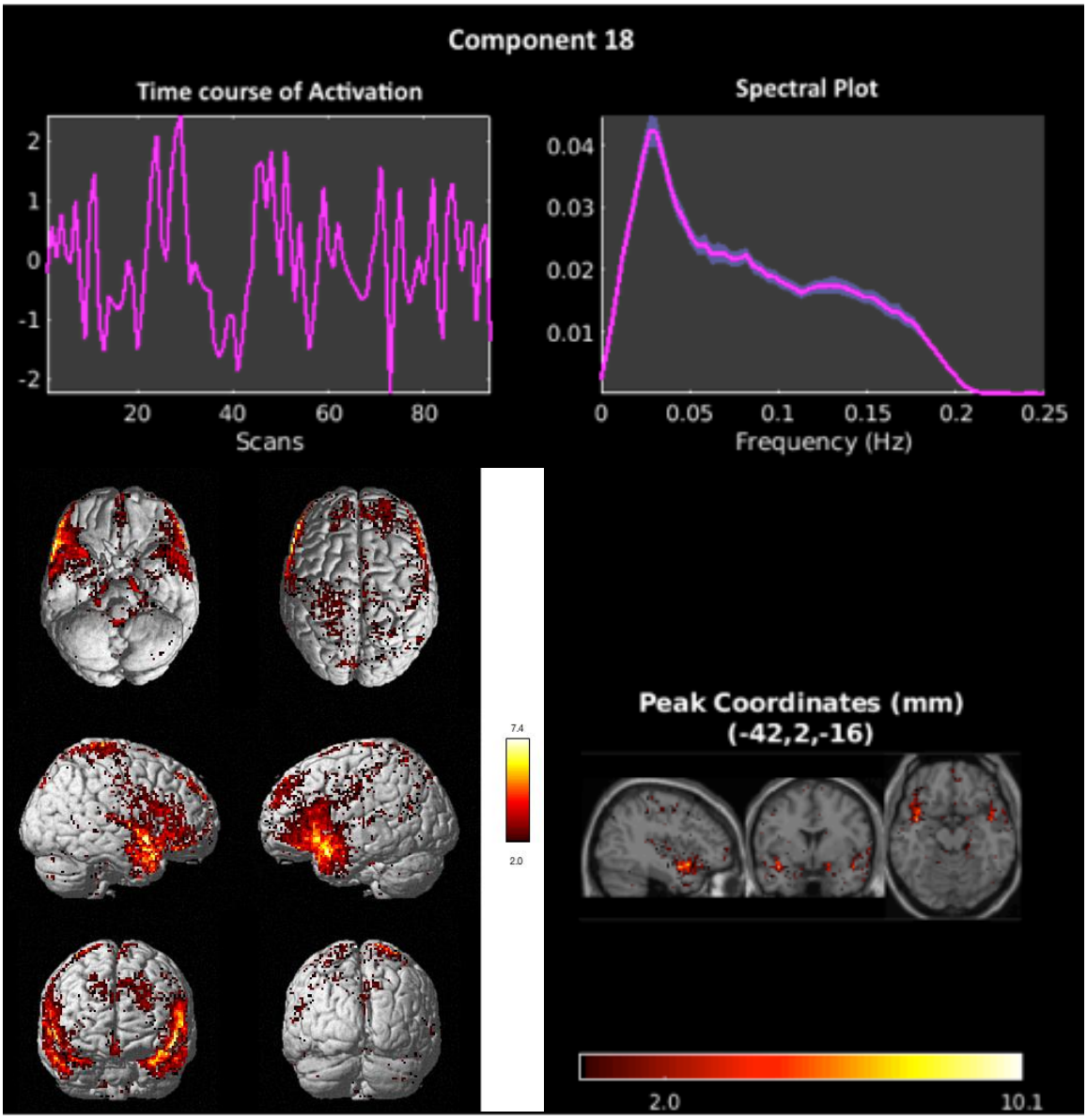

Appendix B Images of the 20 Estimated Components

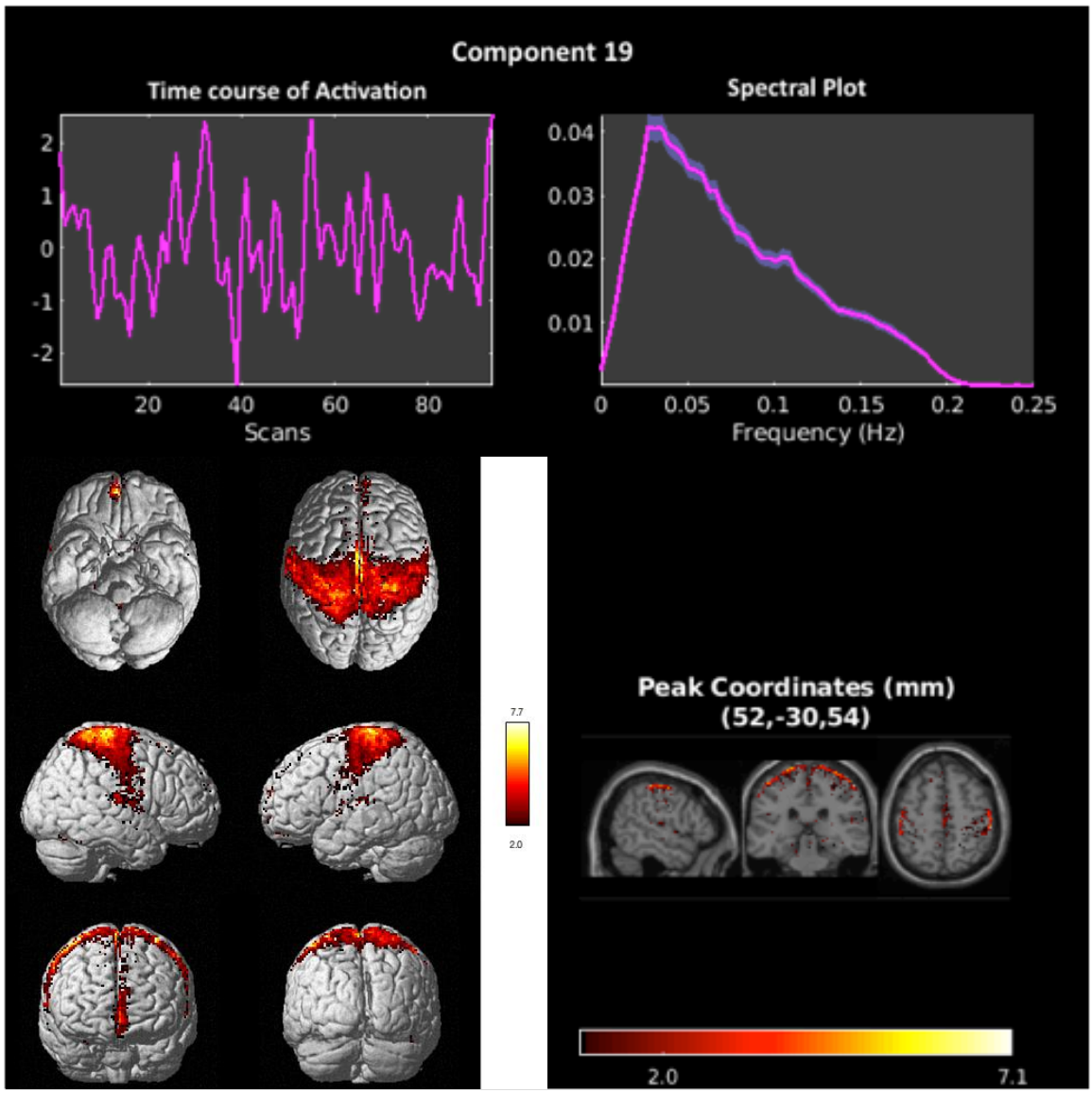

Appendix B Images of the 20 Estimated Components

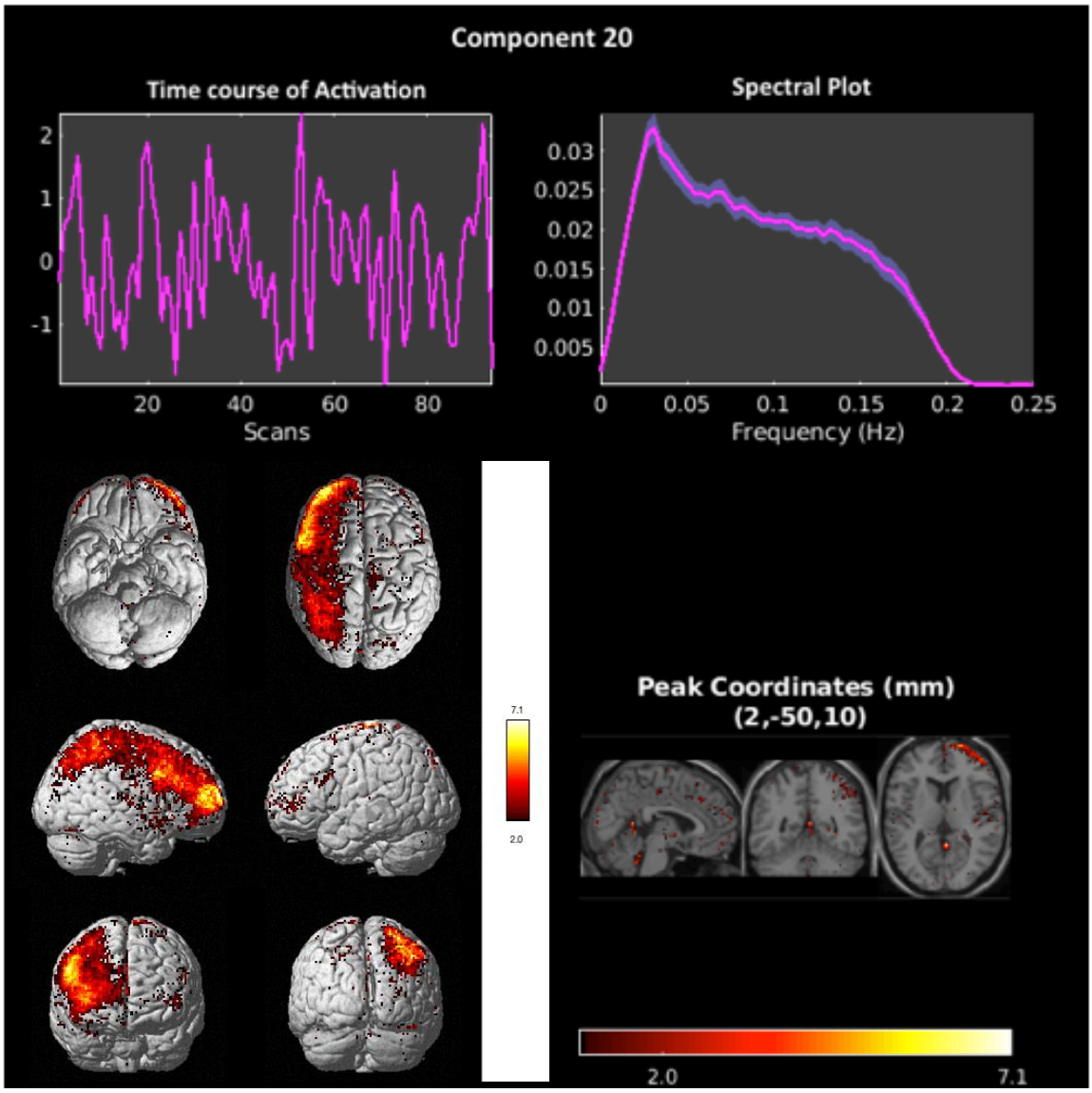

Appendix C Summary Statistics of Regression Model P Values

False Discovery Rate-adjusted p values of the coefficients on the "months since diagnosis" variable in the voxel-wise regression models. Histograms of regression output from a few sample components follow.

Comp # (j)	Minimum	1st Qtr	Median	Mean	3rd Qtr	Maximum
1	0.185	0.846	0.928	0.893	0.971	1.000
2	1.000	1.000	1.000	1.000	1.000	1.000
3	0.092	0.740	0.869	0.822	0.950	1.000
4	0.265	0.897	0.953	0.932	0.982	1.000
5	1.000	1.000	1.000	1.000	1.000	1.000
6	1.000	1.000	1.000	1.000	1.000	1.000
7	1.000	1.000	1.000	1.000	1.000	1.000
8	0.103	0.906	0.955	0.933	0.981	1.000
9	0.086	0.974	0.986	0.978	0.996	1.000
10	0.061	0.933	0.970	0.951	0.988	1.000
11	0.051	0.863	0.930	0.903	0.975	1.000
12	0.549	1.000	1.000	1.000	1.000	1.000
13	0.352	0.904	0.953	0.931	0.983	1.000
14	0.027	0.904	0.953	0.931	0.981	1.000
15	0.442	0.998	0.999	0.998	1.000	1.000
16	0.403	0.888	0.946	0.919	0.980	1.000
17	0.986	0.998	0.998	0.998	1.000	1.000
18	0.374	0.974	0.988	0.979	0.997	1.000
19	0.189	0.843	0.924	0.891	0.969	1.000
20	0.050	0.918	0.963	0.942	0.988	1.000

Appendix C Regression Model Output

Histograms of unadjusted and FDR-adjusted p values from regression model coefficients of two sample components

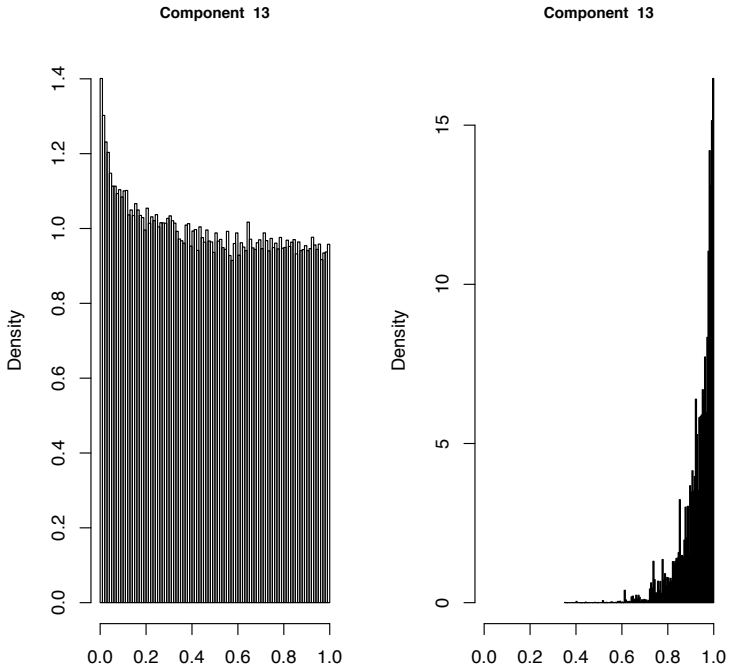

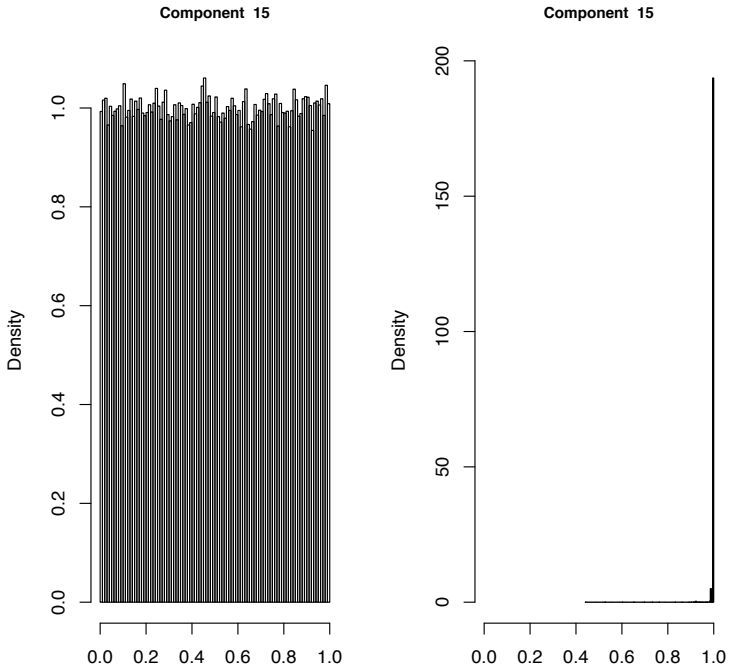

Appendix D Table of Study Results

Summary of Component-Related Results

#	Image Concerns		Differences between Groups	Overlap with Areas in the Basal Ganglia		
	Possible Noise	Spectral Analysis Issues	Histograms Differ	Max Active Voxel (rank/t stat)	Correlation (rank/corr)	Component Labeler
1	Movement		X	9 / 3.01		
2		Interference		2 / 4.55		
3	Movement					
4	Movement	Interference				
5		Interference		4 / 4.16		
6			X	5 / 5.25		
7			X	6 / 3.23		
8						
9			X		4 / 0.007	
10						
11		Possible			2 / 0.014	
12			X		5 / 0.006	
13				1 / 4.63		Corr: 0.091
14					7 / 0.005	
15			X	3 / 4.43	1 / 0.038	
16			X		3 / 0.009	
17			X	8 / 3.11		
18					6 / 0.006	
19						
20			X	7 / 3.15		

Appendix E Derivation of the FastICA algorithm

Given **x**, we want to find a weight vector, **w** to maximize the negentropy,

$$J(y) \propto (E[H(y)] - E[H(\nu)])^2$$

where $y = w^T x$. For both y and ν, μ=0 and $\sigma^2=1$; this is also subject to the constraint of normalized variance: $E[H(w^T x)^2] = ||w||^2 = 1$. The Karush-Kuhn-Tucker condition gives the LaGrangian equation:

$$\nabla E[H(\mathbf{w}^T\mathbf{x})] = -\lambda \nabla ||\mathbf{w}||$$

or

$$E[\mathbf{x}H'(\mathbf{w}^T\mathbf{x})] + \lambda w = 0$$

Newton's iteration method to find an approximate solution of f(**w**)=0, gives the updating formula: $\mathbf{w^*} = \mathbf{w} - \frac{f(w)}{f'(w)}$ where f(**w**) here is $= E[\mathbf{x}H'(\mathbf{w}^T\mathbf{x})] + \lambda w = 0$

$$\frac{\partial f}{\partial \mathbf{w}} = E[\mathbf{x}\mathbf{x}^T H''(\mathbf{w}^T\mathbf{x})] + \lambda$$

which can be approximated as $E[\mathbf{x}\mathbf{x}^T]E[H''(\mathbf{w}^T\mathbf{x})] + \lambda$.

Since the data has been whitened, $E[\mathbf{x}\mathbf{x}^T] = \mathbf{I}$ and this becomes

$$E[H''(w^T z)]\mathbf{I} + \lambda \mathbf{I}.$$

This matrix is now diagonal so it can be inverted. Newton's equation becomes

$$\mathbf{w^*} = \mathbf{w} - \frac{E[\mathbf{x}H'(\mathbf{w}^T\mathbf{x})] + \lambda \mathbf{w}}{E[H''(\mathbf{w}^T\mathbf{x})] + \lambda}$$

to simplify this, both sides can be multiplied by the negative of the denominator

$$\begin{aligned} \mathbf{w^*} &= -\mathbf{w}(E[H''(\mathbf{w}^T\mathbf{x})] + \lambda) + E[\mathbf{x}H'(\mathbf{w}^T\mathbf{x})] + \lambda \mathbf{w}] \\ &= E[\mathbf{x}H'(\mathbf{w}^T\mathbf{x})] - E[H''(\mathbf{w}^T\mathbf{x})]\mathbf{w} \end{aligned}$$

after finding the maximal weight vector, **w**, renormalize:

$$\mathbf{w} = \frac{\mathbf{w^*}}{||\mathbf{w^*}||}$$

Appendix E Histograms of Activation Levels Between Study Groups

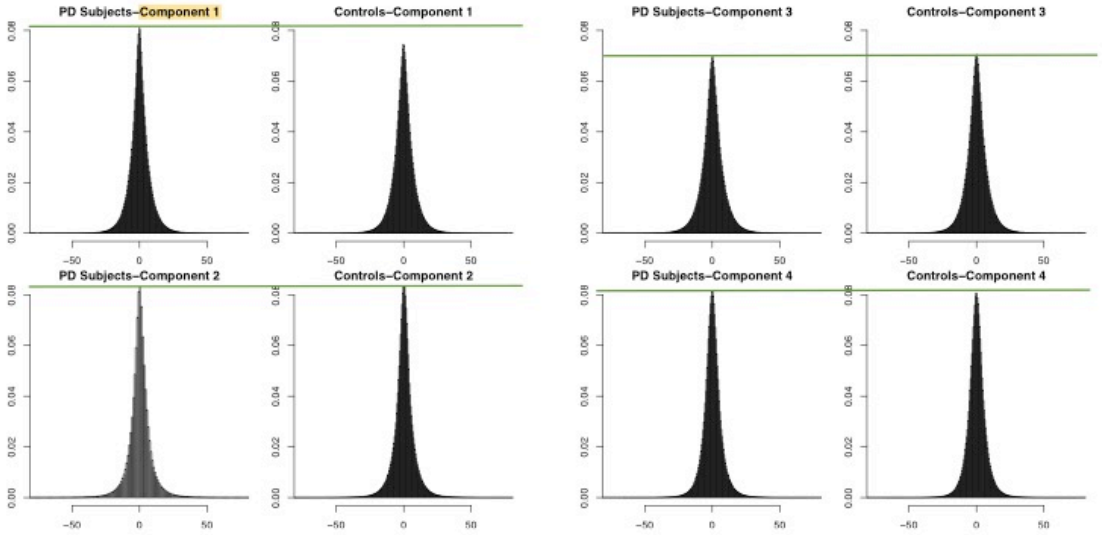

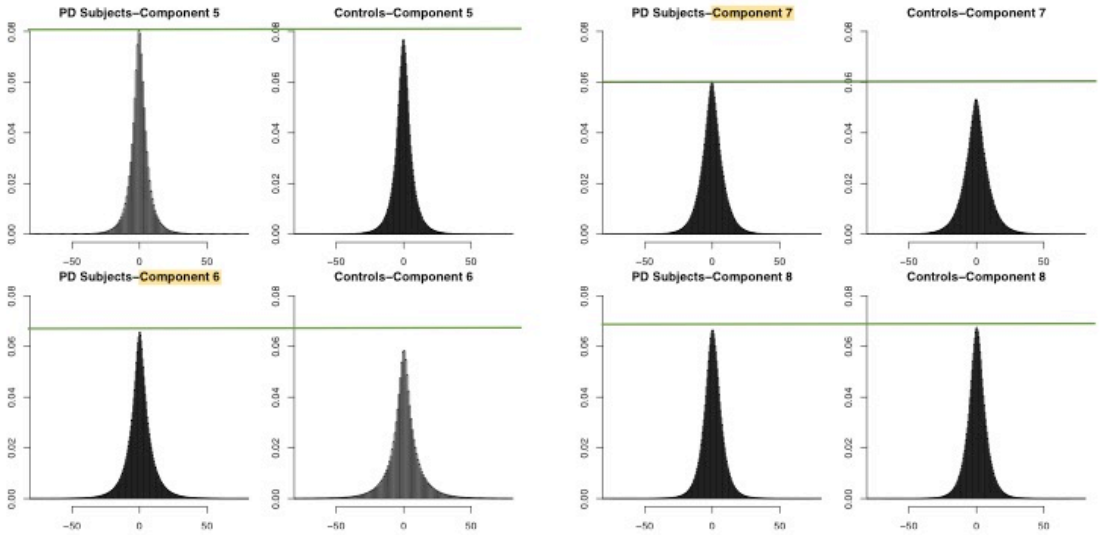

Appendix E Histograms of Activation Levels Between Study Groups

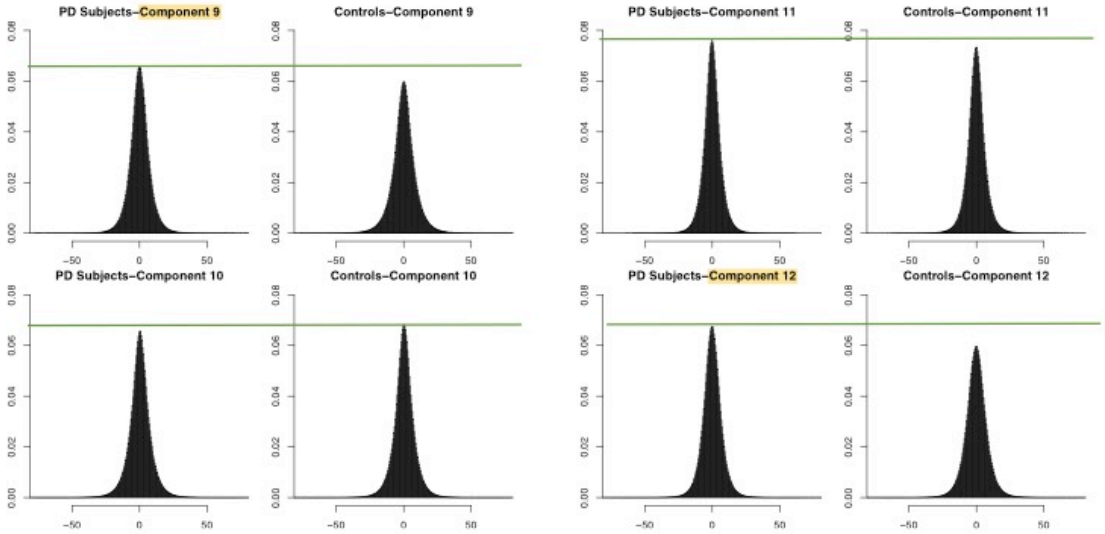

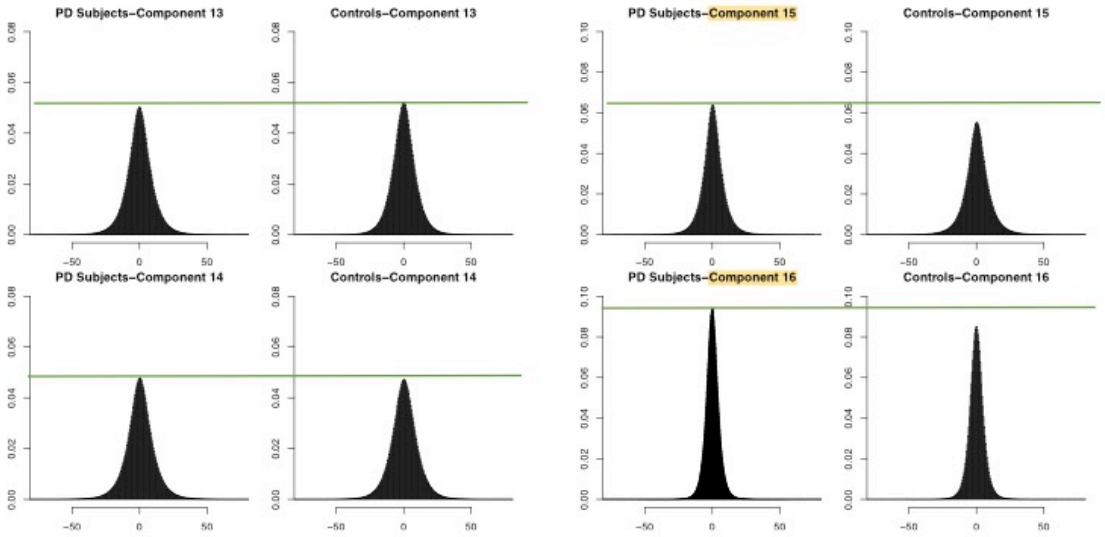

Appendix E Histograms of Activation Levels Between Study Groups

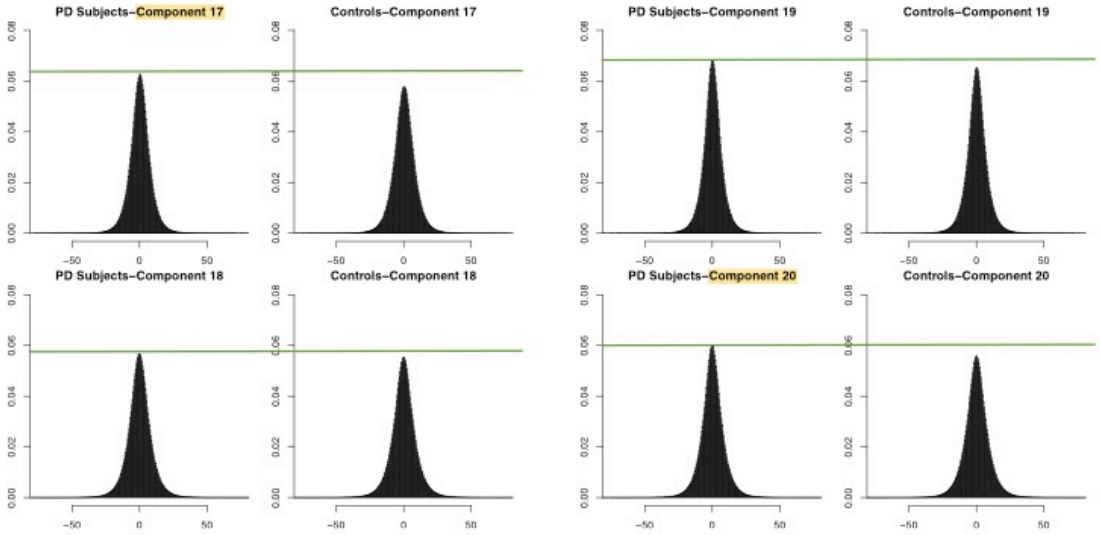

Appendix F Labeled components

Comp#	Label	Max correlation w.r.t template
1	Right DLPFC Parietal (Right Executive Control Network)	0.2642
2	PCC / MPFC (Dorsal Default Mode Network)	0.1660
3	Left DLPFC / Parietal (Left Executive Control Network)	0.0643
4	Retrosplenial Cortex / Medial Temporal Lobe (Ventral Default Mode Network)	0.1377
5	PCC / MPFC (Dorsal Default Mode Network)	0.0993
6	Right DLPFC / Parietal (Right Executive Control Network)	0.0965
7	PCC / MPFC (Dorsal Default Mode Network)	0.1029
8	Retrosplenial Cortex / Medial Temporal Lobe (Ventral Default Mode Network)	0.2042
9	PCC / MPFC (Dorsal Default Mode Network)	0.3830
10	Retrosplenial Cortex / Medial Temporal Lobe (Ventral Default Mode Network)	0.1862
11	Precuneus Network	0.2559
12	Retrosplenial Cortex / Medial Temporal Lobe (Ventral Default Mode Network)	0.1469
13	Basal Ganglia Network	0.0905
14	Posterior Insula (Posterior Salience Network)	0.1376
15	Right DLPFC / Parietal (Right Executive Control Network)	0.1232
16	PCC / MPFC (Dorsal Default Mode Network)	0.1901
17	Left DLPFC / Parietal (Left Executive Control Network)	0.1757
18	Anterior Insula / Dorsal ACC (Anterior Salience Network)	-0.0992
19	Sensorimotor Network	0.1579
20	Right DLPFC / Parietal (Right Executive Control Network)	0.1641

The row shading reflects the amount of correlation between the component and the respective brain region: blue shading: correlation ≥ 0.1; darker blue shading indicates correlation ≥ 0.2. Component 13 was mapped to the basal ganglia, although with correlation < 0.1.

.

References

Allen, Elena A, Erik B. Erhardt, Eswar Damaraju, William Gruner, Judith M. Segall, Rogers F. Silva, Martin Havlicek, et al. 2011. "A Baseline for the Multivariate Comparison of Resting-State Networks," 5, 5 (February): 1–23. https://doi.org/10.3389/fnsys.2011.00002.

Beckmann, Christian F. 2012. "Modelling with Independent Components," NeuroImage 62, 62 (2): 891–901. https://doi.org/10.1016/j.neuroimage.2012.02.020.

Beckmann, Christian F., Clare E. Mackay, N. Filippini, and Stephen M. Smith. 2009. "Group Comparison of Resting-State FMRI Data Using Multi-Subject ICA and Dual Regression." NeuroImage 47. https://doi.org/10.1016/S1053-8119(09)71511-3.

Beckmann, Christian F., Marilena DeLuca, Joseph T. Devlin, and Stephen M. Smith. 2005. "Investigations into Resting-State Connectivity Using Independent Component Analysis," Philosophical Transactions: Biological Sciences 360, 360 (1457): 1001–13. https://doi.org/10.1098/rsbt.2005.1634.

Beckmann, Christian F., Marilena DeLuca, Joseph T. Devlin, and Stephen M. Smith. 2005. "Investigations into Resting-State Connectivity Using Independent Component Analysis," Philosophical Transactions: Biological Sciences 360, 360 (1457): 1001–13. https://doi.org/10.1098/rsbt.2005.1634.

Bell, Anthony J, and Terrence J Sejnowski. 1995. "An Information-Maximization Approach to Blind Separation and Blind Deconvolution," Neural Computation 7, 7 (6): 1129–59. https://doi.org/10.1162/neco.1995.7.6.1129.

Bijsterbosch, Janine, Stephen Smith, Christian Beckmann, and FMRIB Analysis Group. 2018. "Resting State FMRI and ICA." FSL Presentation. Oxford. http://fsl.fmrib.ox.ac.uk/fslcourse/lectures/melodic.pdf.

Bordier, Cé, Michel Dojat, and de Micheaux Lafaye. 2009. *AnalyzeFMRI: An R Package to Perform Statistical Analysis on FMRI Datasets*.

Calhoun, Vince D, Tülay Adali, G. D Pearlson, and J. J Pekar. 2001. "A Method for Making Group Inferences from Functional MRI Data Using Independent Component Analysis," Human Brain Mapping 14, 14 (3): 140–51. https://doi.org/10.1002/hbm.1048.

Calhoun, Vince D, and Tülay Adali. 2006. "Unmixing FMRI with Independent Component Analysis - Using ICA to Characterize High-Dimensional FMRI Data in a Concise Manner,"

Ieee Engineering in Medicine and Biology Magazine 25, 25 (2): 79–90. https://doi.org/10.1109/MEMB.2006.1607672.

Calhoun, Vince D., and Tülay Adali. 2012. "Multisubject Independent Component Analysis of FMRI: A Decade of Intrinsic Networks, Default Mode, and Neurodiagnostic Discovery," IEEE Reviews in Biomedical Engineering 5, 5: 60–73. https://doi.org/10.1109/RBME.2012.2211076.

Calhoun, Vince, and Srinivas Rachakonda. 2018. *Group ICA/IVA of FMRI Toolbox (GIFT)*. University of New Mexico.

Ce, Ji, Yu Yang, and Yu Peng. 2010. "A New FastICA Algorithm of Newton's Iteration." In , 3:V3-481-V3-484. 3. https://doi.org/10.1109/ICETC.2010.5529496.

Chou, Ying-hui. ., L. P. Panych, C. C. Dickey, J. R. Petrella, and N-K. Chen. 2012. "Investigation of Long-Term Reproducibility of Intrinsic Connectivity Network Mapping: A Resting-State FMRI Study," American Journal of Neuroradiology 33, 33 (5): 833–38. https://doi.org/10.3174/ajnr.A2894.

Chou, Ying-hui. 2018. "Parkinson's Study Data," April 2018.

Chou, Ying-hui, Mark Sundman, Heather E Whitson, Pooja Gaur, Mei-lan Chu, Carol P Weingarten, David J Madden, et al. 2017. "Maintenance and Representation of Mind Wandering during Resting-State FMRI," Scientific Reports (Nature Publisher Group) 7, 7: 40722. https://doi.org/10.1038/srep40722.

Cichocki, Andrzej. 2014. *Chapter 21 - Unsupervised Learning Algorithms and Latent Variable Models: PCA/SVD, CCA/PLS, ICA, NMF, Etc*. Edited by Paulo S. R. Diniz, Johan A. K. Suykens, Rama Chellappa, and Sergios Theodoridis. Vol. 1. Academic Press Library in Signal Processing 1. Elsevier. https://doi.org///doi.org/10.1016/B978-0-12-396502-8.00021-8.

Cohen, Jonathan D, Nathaniel Daw, Barbara Engelhardt, Uri Hasson, Kai Li, Yael Niv, Kenneth A Norman, et al. 2017. "Computational Approaches to FMRI Analysis," Nature neuroscience 20, 20 (3): 304–13. https://doi.org/10.1038/nn.4499.

Cole, David M, Stephen M Smith, and Christian F Beckmann. 2010. *Advances and Pitfalls in the Analysis and Interpretation of Resting-State FMRI Data.* Vol. 4. Frontiers in Systems Neuroscience 4. https://doi.org/10.3389/fnsys.2010.00008.

References

Comon, Pierre. 1994. “Independent Component Analysis, A New Concept?” Signal Processing 36. https://doi.org///doi-org.ezproxy1.library.arizona.edu/10.1016/0165-1684(94)90029-9 ".

de Vos, Frank, Marisa Koini, Tijn M. Schouten, Stephan Seiler, der Grond van, Anita Lechner, Reinhold Schmidt, Mark de Rooij, and Serge A. R. B. Rombouts. 2018. “A Comprehensive Analysis of Resting State FMRI Measures to Classify Individual Patients with Alzheimer’s Disease,” NeuroImage 167, 167: 62–72. https://doi.org///doi.org/10.1016/j.neuroimage.2017.11.025.

Eloyan, Ani, Shanshan Li, John Muschelli, Jim J Pekar, Stewart H Mostofsky, and Brian S Caffo. 2014. “Analytic Programming with FMRI Data: A Quick-Start Guide for Statisticians Using R,” PLoS One 9, 9 (2): e89470. https://doi.org/10.1371/journal.pone.0089470.

Erhardt, Erik Barry, Srinivas Rachakonda, Edward J Bedrick, Elena A Allen, Tülay Adali, and Vince D Calhoun. 2011. “Comparison of Multi-Subject ICA Methods for Analysis of FMRI Data,” Human brain mapping 32, 32 (12): 2075–95. https://doi.org/10.1002/hbm.21170.

Esposito, F, E Formisano, E Seifritz, R Goebel, R Morrone, G Tedeschi, and F Di Salle. 2002. “Spatial Independent Component Analysis of Functional MRI Time-Series: To What Extent Do Results Depend on the Algorithm Used?,” Human brain mapping 16, 16 (3): 146–57. https://doi.org/10.1002/hbm.10034.

Filippi, Massimo, Sarasso Elisabetta, Noemi Piramide, and Federica Agosta. 2018. “Functional MRI in Idiopathic Parkinson’s Disease,” International review of neurobiology 141, 141: 439. https://www.ncbi.nlm.nih.gov/pubmed/30314606.

Green, Christopher G., Victor Haughton, and Dietmar Cordes. 2006. *Independent Component Analysis and FMRI Imaging* . Edited by Scott H Faro and Feroze B Mohamed. Functional MRI: Basic Principles and Clinical Applications. New York, NY: Springer.

Greicius, Michael D., Ben Krasnow, Allan L. Reiss, and Vinod Menon. 2003. “Functional Connectivity in the Resting Brain: A Network Analysis of the Default Mode Hypothesis,” Proceedings of the National Academy of Sciences of the United States of America 100, 100 (1): 253–58. https://doi.org/10.1073/pnas.0135058100.

Griffanti, Ludovica, Gwenaëlle Douaud, Janine Bijsterbosch, Stefania Evangelisti, Fidel Alfaro-Almagro, Matthew F Glasser, Eugene P Duff, et al. 2017. “Hand Classification of FMRI ICA Noise Components,” NeuroImage 154, 154 (July): 188–205. https://doi.org/10.1016/j.neuroimage.2016.12.036.

References

Grimm, Laurence G. 1995. *Reading and Understanding Multivariate Statistics*. Washington, DC: American Psychological Assoc.

Hyvärinen, Aapo. 1997a. "A Family of Fixed-Point Algorithms for Independent Component Analysis." In , 5:3917–20 vol.5. 1997 IEEE International Conference on Acoustics, Speech, and Signal Processing 5. IEEE. https://doi.org/10.1109/ICASSP.1997.604766.

———. 1997b. "One-Unit Contrast Functions for Independent Component Analysis: A Statistical Analysis." In , 388–97. Neural Networks for Signal Processing VII. Proceedings of the 1997 IEEE Signal Processing Society Workshop. IEEE. https://doi.org/10.1109/NNSP.1997.622420.

———. 1999. "Fast and Robust Fixed-Point Algorithms for Independent Component Analysis," IEEE Transactions on Neural Networks 10, 10 (3): 626–34.

———. 2013. "Independent Component Analysis: Recent Advances," Philosophical Transactions: Mathematical, Physical and Engineering Sciences 371, 371 (1984): 1–19. https://doi.org/10.1098/rsta.2011.0534.

———. 2015. "Unsupervised Machine Learning Lecture Notes." University of Helsinki.

Hyvärinen, Aapo, Juha Karhunen, and Erkki Oja. 2001. *Independent Component Analysis*. New York: J. Wiley.

Hyvärinen, Aapo, and Erkki Oja. 2000. "Independent Component Analysis: Algorithms and Applications," Neural Networks 13, 13 (4): 411–30.

Joliffe, I. T., and Bjt Morgan. 1992. "Principal Component Analysis and Exploratory Factor Analysis," Stat Methods Med Res 1, 1 (1): 69–95. https://doi.org/10.1177/096228029200100105.

Kim, Junghi, Jeffrey R Wozniak, Bryon A Mueller, Xiaotong Shen, and Wei Pan. 2014. "Comparison of Statistical Tests for Group Differences in Brain Functional Networks," NeuroImage 101, 101 (November): 681–94. https://doi.org/10.1016/j.neuroimage.2014.07.031.

Kim, Paul. n.d. "Direct and Indirect Pathways of the Basal Ganglia." Kenhub. Accessed December 5, 2019. https://www.kenhub.com/en/library/anatomy/direct-and-indirect-pathways-of-the-basal-ganglia.

References

Kiviniemi, Vesa, Juha-Heikki Kantola, Jukka Jauhiainen, Aapo Hyvärinen, and Osmo Tervonen. 2003. "Independent Component Analysis of Nondeterministic FMRI Signal Sources," Neuroimage 19, 19 (2): 253–60. https://doi.org/10.1016/S1053-8119(03)00097-1.

Liu, Thomas T. 2013. "Neurovascular Factors in Resting-State Functional MRI," NeuroImage 80, 80: 339–48. https://doi.org/10.1016/j.neuroimage.2013.04.071.

McKeown, Martin, Scott Makeig, Greg G Brown, Tzyy-Ping Jung, Sandra S Kindermann, Anthony J Bell, and Terrence J Sejnowski. 1998. "Analysis of FMRI Data by Blind Separation into Independent Spatial Components," Human Brain Mapping 6, 6 (3): 160–88. https://doi.org/AID-HBM5>3.0.CO;2-1.

Micheaux,P., Bordier, C., Dojat, M.,. 2011. "Temporal and Spatial Independent Component Analysis for FMRI Data Sets Embedded in the AnalyzeFMRI R Package," Journal of Statistical Software 44, 44 (9): 1–24. https://doi.org/10.18637/jss.v044.i09.

Monti, Martin M. 2011. "Statistical Analysis of FMRI Time-Series: A Critical Review of the GLM Approach," Frontiers in human neuroscience 5, 5: 28. https://doi.org/10.3389/fnhum.2011.00028.

Muschelli, John. 2016. "Processing FMRI Data in R. April 10, 2016. http://johnmuschelli.com/Neuroimaging_in_R/fmri_proc.html.

Niazy, Rami K., Jingyi Xie, Karla Miller, Christian F. Beckmann, and Stephen M. Smith. 2011. "Spectral Characteristics of Resting State Networks," Progress in brain research 193, 193: 259–76. https://doi.org/10.1016/B978-0-444-53839-0.00017-X.

Nickerson, Lisa D., Stephen M. Smith, Döst Öngür, and Christian F. Beckmann. 2017. "Using Dual Regression to Investigate Network Shape and Amplitude in Functional Connectivity Analyses," Frontiers in Neuroscience 11, 11 (115): 1–18. https://doi.org/10.3389/fnins.2017.00115.

Obeso, J A, C Marin, C Rodriguez-Oroz, J Blesa, B Benitez-Temino, J Mena-Segovia, M Rodriguez, and C W Olanow. 2008. "The Basal Ganglia in Parkinson's Disease: Current Concepts and Unexplained Observations," Annals of Neurology, , December, S30-46. https://doi.org/10.1002/ana.21481 [doi].

Parizh, David. 2002. "Speed of Nerve Impulses." The Physics Factbook. 2002. https://hypertextbook.com/facts/2002/DavidParizh.shtml.

References

Prodoehl, J, R G Burciu, and D E Vaillancourt. 2014. “Resting State Functional Magnetic Resonance Imaging in Parkinson’s Disease,” Current neurology and neuroscience reports 14, 14 (6): 448-014-0448–6. https://doi.org/10.1007/s11910-014-0448-6 [doi].

Research, Mayo Foundation for Medical Education and. 2018. “Parkinson’s Disease - Symptoms and Causes.” Mayo Clinic. 2018. https://www.mayoclinic.org/diseases-conditions/parkinsons-disease/symptoms-causes/syc-20376055.

Schmithorst, Vincent J., and Scott K. Holland. 2004. “Comparison of Three Methods for Generating Group Statistical Inferences from Independent Component Analysis of Functional Magnetic Resonance Imaging Data,” Journal of Magnetic Resonance Imaging 19, 19 (3): 365–68. https://doi.org/10.1002/jmri.20009.

Shirer, W. R, S Ryali, E Rykhlevskaia, V Menon, and M. D Greicius. 2012. “Decoding Subject-Driven Cognitive States with Whole-Brain Connectivity Patterns,” Cerebral Cortex 22, 22 (1): 158–65. https://doi.org/10.1093/cercor/bhr099.

Smith, Stephen M, et al. 2009. "Towards a functional hierarchy of resting-state networks." Neuroimage 47: S169, https://www.sciencedirect.com/science/article/pii/S1053811909718105.

Stone, James V. 2004. *Independent Component Analysis: A Tutorial Introduction*. Cambridge, Mass.: MIT Press.

Tahmasian, Masoud, Simon B Eickhoff, Kathrin Giehl, Frank Schwartz, Damian M Herz, Alexander Drzezga, Thilo van Eimeren, et al. 2017. “Resting-State Functional Reorganization in Parkinson’s Disease: An Activation Likelihood Estimation Meta-Analysis,” Cortex 92, 92: 119–38. https://doi.org///doi-org.ezproxy2.library.arizona.edu/10.1016/j.cortex.2017.03.016.

R Core Team. 2018. *R Programming: Language and Environment for Statistical Computing and Data Visualization*. R Foundation for Statistical Computing, Vienna, Austria. www.R-project.org.

Wei, Tianwen. 2014. “On the Spurious Solutions of the Fastica Algorithm.” In , 161–64. 2014 IEEE Workshop on Statistical Signal Processing (SSP). IEEE. https://doi.org/10.1109/SSP.2014.6884600.

References

Whitcher, Brandon, Volker J Schmid, and Andrew Thornton. 2011. “Working with the DICOM and NIfTI Data Standards in R,” Journal of Statistical Software 44, 44 (6). https://doi.org/10.18637/jss.v044.i06.

Woolrich, Mark W., Christian F. Beckmann, Thomas E. Nichols, and Stephen M. Smith. 2016. *Statistical Analysis of FMRI Data*. Edited by Massimo Filippi. FMRI Techniques and Protocols. New York, NY: Springer New York. https://doi.org/10.1007/978-1-4939-5611-1_7.

OXFORD UNIVERSITY PRESS LICENSE
TERMS AND CONDITIONS

Jun 13, 2019

This Agreement between Kirsten Yaffe ("You") and Oxford University Press ("Oxford University Press") consists of your license details and the terms and conditions provided by Oxford University Press and Copyright Clearance Center.

License Number	4607160513418
License date	Jun 13, 2019
Licensed content publisher	Oxford University Press
Licensed content publication	Cerebral Cortex
Licensed content title	Decoding Subject-Driven Cognitive States with Whole-Brain Connectivity Patterns
Licensed content author	Shirer, W. R.; Ryali, S.
Licensed content date	May 26, 2011
Type of Use	Thesis/Dissertation
Institution name	
Title of your work	Independent Component Analysis for Group Comparison of fMRI Images in Parkinson's Disease
Publisher of your work	University of Arizona
Expected publication date	Jun 2019
Permissions cost	0.00 USD
Value added tax	0.00 USD
Total	0.00 USD
Title	Independent Component Analysis for Group Comparison of fMRI Images in Parkinson's Disease
Institution name	University of Arizona
Expected presentation date	Jun 2019
Portions	Supplemental Figure: S2
Requestor Location	Kirsten Yaffe 1295 N Martin Ave. TUCSON, AZ 85724 United States Attn: Kirsten Yaffe
Publisher Tax ID	GB125506730
Total	0.00 USD
Terms and Conditions	

STANDARD TERMS AND CONDITIONS FOR REPRODUCTION OF MATERIAL FROM AN OXFORD UNIVERSITY PRESS JOURNAL

1. Use of the material is restricted to the type of use specified in your order details.
2. This permission covers the use of the material in the English language in the following territory: world. If you have requested additional permission to translate this material, the terms and conditions of this reuse will be set out in clause 12.
3. This permission is limited to the particular use authorized in (1) above and does not allow you to sanction its use elsewhere in any other format other than specified above, nor does it apply to quotations, images, artistic works etc that have been reproduced from other sources which may be part of the material to be used.
4. No alteration, omission or addition is made to the material without our written consent. Permission must be re-cleared with Oxford University Press if/when you decide to reprint.
5. The following credit line appears wherever the material is used: author, title, journal, year, volume, issue number, pagination, by permission of Oxford University Press or the sponsoring society if the journal is a society journal. Where a journal is being published on behalf of a learned society, the details of that society must be included in the credit line.
6. For the reproduction of a full article from an Oxford University Press journal for whatever purpose, the corresponding author of the material concerned should be informed of the proposed use. Contact details for the corresponding authors of all Oxford University Press journal contact can be found alongside either the abstract or full text of the article concerned, accessible from www.oxfordjournals.org Should there be a problem clearing these rights, please contact journals.permissions@oup.com
7. If the credit line or acknowledgement in our publication indicates that any of the figures, images or photos was reproduced, drawn or modified from an earlier source it will be necessary for you to clear this permission with the original publisher as well. If this permission has not been obtained, please note that this material cannot be included in your publication/photocopies.
8. While you may exercise the rights licensed immediately upon issuance of the license at the end of the licensing process for the transaction, provided that you have disclosed complete and accurate details of your proposed use, no license is finally effective unless and until full payment is received from you (either by Oxford University Press or by Copyright Clearance Center (CCC)) as provided in CCC's Billing and Payment terms and conditions. If full payment is not received on a timely basis, then any license preliminarily granted shall be deemed automatically revoked and shall be void as if never granted. Further, in the event that you breach any of these terms and conditions or any of CCC's Billing and Payment terms and conditions, the license is automatically revoked and shall be void as if never granted. Use of materials as described in a revoked license, as well as any use of the materials beyond the scope of an unrevoked license, may constitute copyright infringement and Oxford University Press reserves the right to take any and all action to protect its copyright in the materials.
9. This license is personal to you and may not be sublicensed, assigned or transferred by you to any other person without Oxford University Press's written permission.
10. Oxford University Press reserves all rights not specifically granted in the combination of (i) the license details provided by you and accepted in the course of this licensing transaction, (ii) these terms and conditions and (iii) CCC's Billing and Payment terms and conditions.
11. You hereby indemnify and agree to hold harmless Oxford University Press and CCC, and

their respective officers, directors, employs and agents, from and against any and all claims arising out of your use of the licensed material other than as specifically authorized pursuant to this license.
12. Other Terms and Conditions:
v1.4

Questions? customercare@copyright.com or +1-855-239-3415 (toll free in the US) or +1-978-646-2777.

JOHN WILEY AND SONS LICENSE
TERMS AND CONDITIONS

Jan 09, 2020

This Agreement between Kirsten Yaffe ("You") and John Wiley and Sons ("John Wiley and Sons") consists of your license details and the terms and conditions provided by John Wiley and Sons and Copyright Clearance Center.

License Number	4730570148609
License date	Dec 15, 2019
Licensed Content Publisher	John Wiley and Sons
Licensed Content Publication	Human Brain Mapping
Licensed Content Title	Analysis of fMRI data by blind separation into independent spatial components
Licensed Content Author	Terrence J. Sejnowski, Anthony J. Bell, Sandra S. Kindermann, et al
Licensed Content Date	Dec 7, 1998
Licensed Content Volume	6
Licensed Content Issue	3
Licensed Content Pages	29
Type of use	Dissertation/Thesis

Article citation authors: Martin J. McKeown, Scott Makeig, Greg G. Brown, Tzyy-Ping Jung, Sandra S. Kindermann, Anthony J. Bell, and Terrence J. Sejnowski1

Requestor type	University/Academic
Format	Print and electronic
Portion	Figure/table
Number of figures/tables	4
Original Wiley figure/table number(s)	Figs 2, 3, 15, 16
Will you be translating?	No
Title of your thesis / dissertation	Independent Component Analysis for Group Comparison of fMRI Images in Parkinson's Disease
Expected completion date	Jun 2019
Expected size (number of pages)	60
Requestor Location	Kirsten Yaffe 1295 N Martin Ave. TUCSON, AZ 85724 United States Attn: Kirsten Yaffe
Publisher Tax ID	EU826007151
Total	0.00 USD
Terms and Conditions	

TERMS AND CONDITIONS

This copyrighted material is owned by or exclusively licensed to John Wiley & Sons, Inc. or one of its group companies (each a"Wiley Company") or handled on behalf of a society with which a Wiley Company has exclusive publishing rights in relation to a particular work (collectively "WILEY"). By clicking "accept" in connection with completing this licensing transaction, you agree that the following terms and conditions apply to this transaction (along with the billing and payment terms and conditions established by the Copyright Clearance Center Inc., ("CCC's Billing and Payment terms and conditions"), at the time that you opened your RightsLink account (these are available at any time at http://myaccount.copyright.com).

Terms and Conditions

- The materials you have requested permission to reproduce or reuse (the "Wiley Materials") are protected by copyright.
- You are hereby granted a personal, non-exclusive, non-sub licensable (on a stand-alone basis), non-transferable, worldwide, limited license to reproduce the Wiley Materials for the purpose specified in the licensing process. This license, **and any CONTENT (PDF or image file) purchased as part of your order,** is for a one-time use only and limited to any maximum distribution number specified in the license. The first instance of republication or reuse granted by this license must be completed within two years of the date of the grant of this license (although copies prepared before the end date may be distributed thereafter). The Wiley Materials shall not be used in any other manner or for any other purpose, beyond what is granted in the license. Permission is granted subject to an appropriate acknowledgement given to the author, title of the material/book/journal and the publisher. You shall also duplicate the copyright notice that appears in the Wiley publication in your use of the Wiley Material. Permission is also granted on the understanding that nowhere in the text is a previously published source acknowledged for all or part of this Wiley Material. Any third party content is expressly excluded from this permission.
- With respect to the Wiley Materials, all rights are reserved. Except as expressly granted by the terms of the license, no part of the Wiley Materials may be copied, modified, adapted (except for minor reformatting required by the new Publication), translated, reproduced, transferred or distributed, in any form or by any means, and no derivative works may be made based on the Wiley Materials without the prior permission of the respective copyright owner.**For STM Signatory Publishers clearing permission under the terms of the STM Permissions Guidelines only, the terms of the license are extended to include subsequent editions and for editions in other languages, provided such editions are for the work as a whole in situ and does not involve the separate exploitation of the permitted figures or extracts,** You may not alter, remove or suppress in any manner any copyright, trademark or other notices displayed by the Wiley Materials. You may not license, rent, sell, loan, lease, pledge, offer as security, transfer or assign the Wiley Materials on a stand-alone basis, or any of the rights granted to you hereunder to any other person.

- The Wiley Materials and all of the intellectual property rights therein shall at all times remain the exclusive property of John Wiley & Sons Inc, the Wiley Companies, or their respective licensors, and your interest therein is only that of having possession of and the right to reproduce the Wiley Materials pursuant to Section 2 herein during the continuance of this Agreement. You agree that you own no right, title or interest in or to the Wiley Materials or any of the intellectual property rights therein. You shall have no rights hereunder other than the license as provided for above in Section 2. No right, license or interest to any trademark, trade name, service mark or other branding ("Marks") of WILEY or its licensors is granted hereunder, and you agree that you shall not assert any such right, license or interest with respect thereto

- NEITHER WILEY NOR ITS LICENSORS MAKES ANY WARRANTY OR REPRESENTATION OF ANY KIND TO YOU OR ANY THIRD PARTY, EXPRESS, IMPLIED OR STATUTORY, WITH RESPECT TO THE MATERIALS OR THE ACCURACY OF ANY INFORMATION CONTAINED IN THE MATERIALS, INCLUDING, WITHOUT LIMITATION, ANY IMPLIED WARRANTY OF MERCHANTABILITY, ACCURACY, SATISFACTORY QUALITY, FITNESS FOR A PARTICULAR PURPOSE, USABILITY, INTEGRATION OR NON-INFRINGEMENT AND ALL SUCH WARRANTIES ARE HEREBY EXCLUDED BY WILEY AND ITS LICENSORS AND WAIVED BY YOU.

- WILEY shall have the right to terminate this Agreement immediately upon breach of this Agreement by you.

- You shall indemnify, defend and hold harmless WILEY, its Licensors and their respective directors, officers, agents and employees, from and against any actual or threatened claims, demands, causes of action or proceedings arising from any breach of this Agreement by you.

- IN NO EVENT SHALL WILEY OR ITS LICENSORS BE LIABLE TO YOU OR ANY OTHER PARTY OR ANY OTHER PERSON OR ENTITY FOR ANY SPECIAL, CONSEQUENTIAL, INCIDENTAL, INDIRECT, EXEMPLARY OR PUNITIVE DAMAGES, HOWEVER CAUSED, ARISING OUT OF OR IN CONNECTION WITH THE DOWNLOADING, PROVISIONING, VIEWING OR USE OF THE MATERIALS REGARDLESS OF THE FORM OF ACTION, WHETHER FOR BREACH OF CONTRACT, BREACH OF WARRANTY, TORT, NEGLIGENCE, INFRINGEMENT OR OTHERWISE (INCLUDING, WITHOUT LIMITATION, DAMAGES BASED ON LOSS OF PROFITS, DATA, FILES, USE, BUSINESS OPPORTUNITY OR CLAIMS OF THIRD PARTIES), AND WHETHER OR NOT THE PARTY HAS BEEN ADVISED OF THE POSSIBILITY OF SUCH DAMAGES. THIS LIMITATION SHALL APPLY NOTWITHSTANDING ANY FAILURE OF ESSENTIAL PURPOSE OF ANY LIMITED REMEDY PROVIDED HEREIN.

- Should any provision of this Agreement be held by a court of competent jurisdiction to be illegal, invalid, or unenforceable, that provision shall be deemed amended to

achieve as nearly as possible the same economic effect as the original provision, and the legality, validity and enforceability of the remaining provisions of this Agreement shall not be affected or impaired thereby.

- The failure of either party to enforce any term or condition of this Agreement shall not constitute a waiver of either party's right to enforce each and every term and condition of this Agreement. No breach under this agreement shall be deemed waived or excused by either party unless such waiver or consent is in writing signed by the party granting such waiver or consent. The waiver by or consent of a party to a breach of any provision of this Agreement shall not operate or be construed as a waiver of or consent to any other or subsequent breach by such other party.
- This Agreement may not be assigned (including by operation of law or otherwise) by you without WILEY's prior written consent.
- Any fee required for this permission shall be non-refundable after thirty (30) days from receipt by the CCC.
- These terms and conditions together with CCC's Billing and Payment terms and conditions (which are incorporated herein) form the entire agreement between you and WILEY concerning this licensing transaction and (in the absence of fraud) supersedes all prior agreements and representations of the parties, oral or written. This Agreement may not be amended except in writing signed by both parties. This Agreement shall be binding upon and inure to the benefit of the parties' successors, legal representatives, and authorized assigns.
- In the event of any conflict between your obligations established by these terms and conditions and those established by CCC's Billing and Payment terms and conditions, these terms and conditions shall prevail.
- WILEY expressly reserves all rights not specifically granted in the combination of (i) the license details provided by you and accepted in the course of this licensing transaction, (ii) these terms and conditions and (iii) CCC's Billing and Payment terms and conditions.
- This Agreement will be void if the Type of Use, Format, Circulation, or Requestor Type was misrepresented during the licensing process.
- This Agreement shall be governed by and construed in accordance with the laws of the State of New York, USA, without regards to such state's conflict of law rules. Any legal action, suit or proceeding arising out of or relating to these Terms and Conditions or the breach thereof shall be instituted in a court of competent jurisdiction in New York County in the State of New York in the United States of America and each party hereby consents and submits to the personal jurisdiction of such court, waives any objection to venue in such court and consents to service of process by registered or certified mail, return receipt requested, at the last known address of such party.

JOHN WILEY AND SONS LICENSE
TERMS AND CONDITIONS

Jan 09, 2020

This Agreement between Kirsten Yaffe ("You") and John Wiley and Sons ("John Wiley and Sons") consists of your license details and the terms and conditions provided by John Wiley and Sons and Copyright Clearance Center.

License Number	4730570148609
License date	Dec 15, 2019
Licensed Content Publisher	John Wiley and Sons
Licensed Content Publication	Human Brain Mapping
Licensed Content Title	Analysis of fMRI data by blind separation into independent spatial components
Licensed Content Author	Terrence J. Sejnowski, Anthony J. Bell, Sandra S. Kindermann, et al
Licensed Content Date	Dec 7, 1998
Licensed Content Volume	6
Licensed Content Issue	3
Licensed Content Pages	29
Type of use	Dissertation/Thesis